

# Fabrication, microstructure and properties of nanoporous Pd, Ni and their alloys by dealloying

Masataka HAKAMADA

5 Department of Energy Science and Technology, Graduate School of Energy Science,  
Kyoto University, Yoshidahonmachi, Sakyo, Kyoto 606-8501, Japan

Tel: +81-75-753-5427; fax: +81-75-753-5428.

E-mail: hakamada.masataka.3x@kyoto-u.ac.jp

10 Mamoru MABUCHI (Corresponding author)

Department of Energy Science and Technology, Graduate School of Energy Science,  
Kyoto University, Yoshidahonmachi, Sakyo, Kyoto 606-8501, Japan

Tel: +81-75-753-5404; fax: +81-75-753-5428.

E-mail: mabuchi@energy.kyoto-u.ac.jp

15

## **Abstract**

Nanoporous metals can be fabricated by dealloying, which is one of the reactions that occur during the corrosion of alloys. Nanoporous gold has been widely investigated for several decades, and it has recently been found that other metals such as platinum, 5 palladium, nickel and copper can form nanoporous structures through the dealloying of binary alloys. This article mainly shows fabrication and properties of nanoporous palladium and nickel after introduction of nanoporous metals by referring to nanoporous gold as an example. It is necessary to select binary alloys with suitable elements, in which the dissolution of the less noble element and the aggregation of the 10 nobler element at the solid/electrolyte interface are simultaneously allowed. Postprocessing by thermal or acid treatment alters the nanoporous structure. Various properties of nanoporous metals (including mechanical, catalytic, piezoelectric, hydrogenation and magnetic ones) are different from those of bulk and nanocrystalline materials and nanoparticles because of their specific three-dimensional network 15 structures consisting of nanosized pores and ligaments. Hydrogenation and magnetic properties are reviewed in terms of lattice strain at curved surfaces. These new metallic nanomaterials are now being investigated from the viewpoint of functional applications, and provide much room for study in various fields.

*Keywords:* nanoporous metals, dealloying, corrosion, pore size, surface

20 **Title for running head:** Nanoporous metals fabricated by dealloying

## Table of contents

	1. Introduction .....	4
	2. Nanoporous gold .....	6
	2.1 Fabrication .....	7
5	2.2 Properties .....	10
	3. Nanoporous palladium.....	12
	3.1 Fabrication .....	12
	3.2 Properties: hydrogen storage .....	17
	4. Nanoporous nickel and nickel-copper .....	21
10	4.1 Fabrication .....	22
	4.2 Properties: magnetism in nanoporous Ni.....	23
	5. Other nanoporous metals .....	25
	6. Surface area determination .....	26
	7. Summary.....	28
15	Acknowledgements .....	29
	References .....	30
	Figure Captions .....	45

## 1. Introduction

Materials with a porous (or foamed or cellular) structure intrinsically provide many functions.<sup>1-5</sup> In particular, nanoporous structures, which consist of a network of nanosized pores and ligaments, are common in oxide ceramics<sup>6-8</sup> and carbon materials,<sup>9,10</sup> and offer several important functions for the synthesis and processing of materials. On the other hand, nanoporous metals with an interconnected open-cell structure can be easily fabricated through self-organization by dealloying,<sup>11-14</sup> which is one of the fundamental corrosion reactions. Nanoporous metals, similarly to other nanoporous materials, have a high surface area and are promising materials for electrode, sensor and catalytic applications. During the last decade, increasing research attention has been paid to nanoporous metals, although the formation of nanoporous structures itself has been known and utilized since the 1920s, during which nanoporous Raney-type catalysts were patented.<sup>15,16</sup>

Figure 1 shows a schematic illustration of the use of dealloying to fabricate nanoporous metals. The scheme is simple and as follows. First, a starting binary alloy is prepared. Second, one of the elements in the starting alloy is selectively dissolved in an electrolyte. During the dissolution of this element, the other element spontaneously forms a nanoporous structure. This spontaneity in dealloying is similar to spinodal decomposition,<sup>12</sup> in which entwined two phases gradually forms without nucleation

and growth during the equilibration of two-elemental solids, and markedly different from the so-called template, replication or spacer method,<sup>17-19</sup> where the pores (in metals and other materials) are created by the removal of spacing materials such as particles and wires from metal-spacer composites. Thus, this self-synthetic nature of nanoporous metals is attractive for the efficient production of high-surface-area metallic components.

The atomic behavior considered to occur at the solid/electrolyte interface during dealloying is schematically shown in Fig. 2, where element A is chemically nobler (more stable) than element B. Two processes are equivalently involved in the formation of nanoporous metals: one is the dissolution of the less noble element B into the solution and the other is the aggregation of the nobler element A at the interface.<sup>11,12</sup> At the initial stage of dealloying of the A-B alloy, B first dissolves into an electrolyte, leaving vacancies and less-coordinated A atoms at the solid surface. Then the less-coordinated, and thus less stable, A atoms diffuse at the interface to form islands consisting of a number of A atoms. The aggregation of A atoms exposes the underlying A-B alloy to the electrolyte, allowing the subsequent dissolution and removal of B. Thus, the repetition of B dissolution and A aggregation at the solid/electrolyte interface results in the final nanoporous structure.

As shown later, the size and morphology of pores and ligaments can be controlled by thermal and/or acid treatments, which induce the reorganization of the

nanoporous structure. Figure 3 shows a comparison of the range of controllable pore and ligament sizes with various substances having submicron-scale length. The smallest pores are under 5 nm while the largest pores are above 1000 nm. The ability to adjust the pore size over such a wide range is one of the characteristics of nanoporous metals fabricated by dealloying.

The fabricated nanoporous metals have a large surface area due to their small ligament sizes. The surface area is almost comparable to that of nanoparticles; however, the interconnected three-dimensional nanoligaments in nanoporous metals are expected to exhibit properties different from those of individual and aggregated nanoparticles.

In this review we review the fabrication of various species of nanoporous metals by dealloying, followed by a description of their properties.

## 2. Nanoporous gold

Dealloying and the subsequent formation of nanopores have been reported most frequently for gold (Au).<sup>11,12</sup> Actually, several good and comprehensive review papers on nanoporous Au have been already published.<sup>13,14,20-23</sup> This is because the investigation of nanoporous Au started much earlier than that of other nanoporous metals. Mechanisms related to the fabrication and properties of nanoporous Au have been thoroughly investigated and are documented well; for further details, see the review papers.<sup>13,14,20-23</sup> In this section, a brief description of nanoporous Au will be

given to only introduce the key fundamentals of nanoporous metals.

## 2.1 Fabrication

A typical initial alloy used for the fabrication of nanoporous Au is Au-Ag since  
5 Ag dissolves into HNO<sub>3</sub> and HClO<sub>4</sub>. Because of the high inertness of Au and the  
sufficiently high solubility of Ag in these electrolytes, which can be understood by the  
comparison of standard electrode potentials ( $E_0(\text{Au}^{3+}/\text{Au}) = +1.50 \text{ V}$  vs standard  
hydrogen electrode (SHE), and  $E_0(\text{Ag}^+/\text{Ag}) = +0.80 \text{ vs SHE}$ ),<sup>24</sup> it is easy to fabricate  
nanoporous Au from Au-Ag alloy. When alloyed with each other, Au and Ag form a  
10 face-centered-cubic (fcc) solid solution at all compositions; hence, the resulting pore  
characteristics such as porosity and pore size can be tuned over a wide range, and the  
discussion of the relationship among the processing conditions, pore characteristics  
and properties of the nanoporous metal is straightforward. The Ag content in the initial  
Au-Ag alloy must be larger than approximately 0.55 for the production of nanoporous  
15 Au;<sup>25</sup> otherwise the dissolution of Ag stops after minimal dissolution of Ag from the  
outermost surface of the alloy. The other combinations of Au-Cu<sup>26,27</sup> and Au-Al<sup>28,29</sup> are  
possible, although these alloys intrinsically contain ordered intermetallic compounds,  
which may make the discussion complicated and limit the range of processing  
conditions.

20 Figures 4–7 shows scanning electron microscopy (SEM) images of various

nanoporous Au structures fabricated by the dealloying of Au-Ag alloy in HNO<sub>3</sub> or HClO<sub>4</sub>.<sup>30–33</sup> These figures clearly demonstrate that the pore size and morphology strongly depend on the processing conditions including the acid or thermal treatments after dealloying.

5           In free corrosion, which is the simplest dealloying technique, the initial Au-Ag alloy is immersed in a concentrated electrolyte such as HNO<sub>3</sub>. Pore and ligament sizes increase with the immersion time, as shown in Fig. 4, owing to the diffusion of Au atoms at the solid/electrolyte interface.<sup>33–35</sup> Free corrosion at lower temperatures leads to smaller pore and ligament sizes (Fig. 4d) because of the suppression of Au atom  
10   diffusion.<sup>35</sup>

          On the other hand, dealloying under an anodic electrochemical potential results in nanoporous structures as fine as 5–10 nm (Fig. 5a). In general, the imposition of a higher anodic potential results in smaller pores.<sup>33,36</sup> The anodic electrochemical potential, in general, causes a significant volume reduction during the dissolution of Ag  
15   and leads to macroscopic crack formation (Fig. 5b).<sup>30,36</sup>

          Careful investigation showed that nanoporous Au can be synthesized by dealloying of Au-Ag in electrolytes with neutral pH under anodic potentials.<sup>37,38</sup> Residual Ag, which can be in the alloyed or oxide forms depending on pH, considerably affects the kinetics of dealloying. As a result, pH of the electrolyte and  
20   potentials are quite important for not only pore/ligament size control but the residual



amount of less noble element.<sup>38</sup> This aspect should be investigated extensively to other initial alloy systems and electrolytes for facile control of nanoporous structure and residual less noble elements.

Acid treatment by concentrated HCl after dealloying under an electrochemical potential leads to the formation of peculiar prislake structures with the nanoporosity coarsened to 300–500 nm (Fig. 6).<sup>30</sup> That is, nanoporous Au prisms with dense walls are created throughout the entire specimen. At the top surface of the specimen, nanoporous walls, whose ligament sizes are increased to 300–500 nm, separate the surface of the specimens into “plots”, whose interiors are hollow (Figs. 6a and 6b). At the bottom surface of the specimens, on the other hand, the nanoporous structure is enclosed inside highly dense walls (Fig. 6c). The ligament size of the inner porous structure is 300–500 nm, and the thickness of the enclosing walls is approximately 1  $\mu\text{m}$ . Each plot has side lengths of 5–20  $\mu\text{m}$  and extends toward the inside of the specimens, forming nanoporous prislake structure with dense walls (Fig. 6d). The dense walls break down further into the sample thickness. These prisms are approximately perpendicular to the specimen surface. The microassembly of nanoporous Au prisms, which is due to heterogeneous coarsening of the porous structure, appears to be related to the macroscopic cracks in the as-dealloyed sample before the HCl treatment (Fig. 5b).

Thermal treatment also coarsens the nanoporous structure,<sup>32,39</sup> while maintaining

the open-cell porous structure. Higher heating temperatures lead to larger pore and ligament diameters (up to 1.2  $\mu\text{m}$ ), as shown in Fig. 7. The thermally-coarsened nanoporous structures with characteristic length scale above approximately 150 nm can be observed by transmission X-ray microscopy.<sup>40</sup> Compared with the melting of nanoparticles at temperatures lower than the melting point of bulk Au,<sup>41</sup> the coarsening of nanoporous Au by thermal treatment alters the nanostructure at much lower temperatures. Differential scanning calorimetry results for nanoporous Au exhibit an exothermic peak (Fig. 8), which indicates that solid-state reorganization processes, rather than melting, are responsible for the coarsening of heated nanoporous Au.

Several observations by transmission electron microscopy (TEM) have revealed that typical nanoporous metals, including coarsened ones, have a grain size much larger than the pore and ligament sizes;<sup>34,36</sup> therefore, the exothermic peak is unlikely to be caused by recrystallization, although the dependence of pore/ligament size on heating temperature is similar to that of the grain size in nanocrystalline Au.<sup>32</sup> Thermal coarsening in nanoporous Au is an efficient means of controlling the pore size over a wide range, although it turns unsuitable when nanoporous Au is to be applied in high-temperature environments.

## 2.2 Properties

Many researchers have revealed peculiar properties of nanoporous Au, which

have already been documented in published papers including review articles.<sup>13,14,20,27,31,39,41–49</sup> For example, the mechanical strength of nanoporous Au increases with decreasing pore and ligament sizes.<sup>28,40</sup> Marked strengthening upon reducing the pore size has not been observed in conventional macroscopic porous materials with millimeter- and micrometer-scale pores and ligaments.<sup>1</sup> This suggests that the dislocation activity, which is responsible for the plastic deformation of metals, is strongly affected by the nanoporous structure. Dou and Derby summarized the mechanical properties of nanoporous Au uncovered by many researchers and emphasized the peculiar microstructures of microtwins and partial dislocations localized at bent nodes in the nanoporous architecture during deformation.<sup>47</sup>

The catalytic properties of nanoporous Au have also been reported, although bulk Au itself is not always a catalytic material.<sup>27,48</sup> The effect of nanosized pores and ligaments with possible surface strain may be similar to the case of Au nanoparticles supported on porous oxides.<sup>50</sup> Kameoka and Tsai reported enhanced CO oxidation on nanoporous Au fabricated by dealloying Au-Cu alloy.<sup>27</sup> Wittstock et al. also revealed CO oxidation on nanoporous Au fabricated by dealloying Au-Ag alloy and attributed the catalytic properties to the residual Ag segregated at the surface.<sup>48</sup> The catalytic effect of nanoporous Au on other reactions such as the oxidation of CH<sub>3</sub>OH has also been reported.<sup>49</sup>

The piezoelectric properties of nanoporous Au, which are related to its large

surface area, become apparent in an electrolyte<sup>51,52</sup> and under an atmosphere of specific gases.<sup>53</sup> This piezoelectric nature of nanoporous materials was originally reported for platinum black<sup>54</sup> and may be useful for applications to sensors and actuators. In addition, nanoporous Au exhibits optical properties including surface-enhanced Raman scattering, which can be used for sensing applications.<sup>13,55-57</sup>

### 3. Nanoporous palladium

Palladium (Pd) is one of the platinum group metals and known for its chemical inertness, catalytic properties and hydrogen storage capacity. Hence, Pd nanostructures (including nanoparticles) with high surface area have been intensively developed for catalytic devices and sensors.<sup>58,59</sup> However, less attention has been paid to the fabrication of nanoporous Pd through dealloying, although Kabius et al. reported its formation by dealloying Pd-Cu alloy in 1986.<sup>60</sup>

#### 3.1 Fabrication

Recently, dealloying of Pd-containing alloys to fabricate nanoporous Pd has been extensively examined by the present authors.<sup>61-63</sup> Iron (Fe), cobalt (Co) and nickel (Ni) were selected as candidates for the sacrificial elements in Pd-containing starting alloys for two reasons; one is that the standard electrode potentials of Fe, Co and Ni are much lower than that of Pd (as summarized in Table 1) and the other is that Fe, Co and Ni

forms single-phase solid solution when alloyed with Pd. However, the anodic polarization behaviors of these alloys, where the alloys were used as working electrodes in H<sub>2</sub>SO<sub>4</sub> electrolyte, significantly differed, as shown in Fig. 9. Pure Fe, Co and Ni exhibited monotonic increases in current with increasing potential and no passivity was observed. This suggests that passive surface oxide films of Fe, Co and Ni do not form upon electrolysis in H<sub>2</sub>SO<sub>4</sub>. Pd<sub>0.2</sub>Co<sub>0.8</sub> alloy also exhibited a similar trend in its anodic polarization curve (Fig. 9(b)), although the measured current was smaller than that of pure Co. The monotonic current increase in the anodic polarization curve of Pd<sub>0.2</sub>Co<sub>0.8</sub> is similar to those for Au-Ag alloys, which produce nanoporous Au upon electrolysis.<sup>64</sup> On the other hand, Pd<sub>0.2</sub>Fe<sub>0.8</sub> and Pd<sub>0.2</sub>Ni<sub>0.8</sub> clearly had regions of passivity at high potentials, at which a low constant current was detected. The constant-potential electrolysis of Pd<sub>0.2</sub>Fe<sub>0.8</sub>, Pd<sub>0.2</sub>Co<sub>0.8</sub> and Pd<sub>0.2</sub>Ni<sub>0.8</sub> in H<sub>2</sub>SO<sub>4</sub> (Fig. 10) showed that a large current was detected during the constant-potential (+0.6 V vs saturated calomel electrode (SCE)) electrolysis of Pd<sub>0.2</sub>Co<sub>0.8</sub>, suggesting the considerable dissolution of Co into the electrolyte; however, very little current was observed in the cases of Pd<sub>0.2</sub>Fe<sub>0.8</sub> and Pd<sub>0.2</sub>Ni<sub>0.8</sub>.

Figures 11 (a)–(c) are the SEM images of Pd<sub>0.2</sub>Fe<sub>0.8</sub>, Pd<sub>0.2</sub>Co<sub>0.8</sub> and Pd<sub>0.2</sub>Ni<sub>0.8</sub> after the constant-potential electrolysis. Pd<sub>0.2</sub>Co<sub>0.8</sub> alloy exhibited an open-cell nanoporous structure (Fig. 11 (b)). The ligament and pore sizes were approximately 20 nm. However, Pd<sub>0.2</sub>Fe<sub>0.8</sub> and Pd<sub>0.2</sub>Ni<sub>0.8</sub> had featureless microstructures after the

electrolysis (Figs. 11 (a) and (c)). The passivity indicated in Fig. 9 clearly prevents the formation of nanopores. Thus, Pd-Co is a promising starting material among the three alloys for fabrication of nanoporous Pd. The compositional effect on the current/potential behavior of Pd-Co alloy ingots in 0.1 mol/l H<sub>2</sub>SO<sub>4</sub> solution is shown in Fig. 12. For all the Pd-Co alloys tested, the current density monotonically increased with the potential increase. Dealloying critical potentials, which can be determined as the potential corresponding to a current density of 1 mA cm<sup>-2</sup>,<sup>64</sup> were +0.17, +0.04 and +0.00 V for Pd<sub>0.2</sub>Co<sub>0.8</sub>, Pd<sub>0.15</sub>Co<sub>0.85</sub> and Pd<sub>0.1</sub>Co<sub>0.9</sub> alloys, respectively. The dealloying critical potential decreased with increasing content of less noble element (Co). This trend is reasonable and agrees with the electrochemical behavior of Au-Ag alloys.<sup>64</sup>

To investigate the mechanism that governs the nanoporosity evolution from the Pd-containing alloys, two surface elemental analyses with different detection depth were conducted on the alloy surfaces before and after the electrolysis. One is energy-dispersive X-ray spectroscopy (EDXS) with typical detection depth of 1–10 μm and the other is X-ray photoelectron spectroscopy (XPS) with the detection depth of < 2 nm; thus EDXS and XPS give the information on bulk and near-surface composition, respectively. EDXS suggested that Co dissolves into H<sub>2</sub>SO<sub>4</sub> from Pd<sub>0.2</sub>Co<sub>0.8</sub> during the constant electrolysis, while bulk composition does not change after the constant electrolysis of Pd<sub>0.2</sub>Fe<sub>0.8</sub> and Pd<sub>0.2</sub>Ni<sub>0.8</sub> (Fig. 13). However, XPS analyses (Fig. 14) showed that Fe and Ni near the surface (within the detection depth of XPS) of

$\text{Pd}_{0.2}\text{Fe}_{0.8}$  and  $\text{Pd}_{0.2}\text{Ni}_{0.8}$  disappear after the electrolysis. XPS also revealed the surface enrichment of Co at the surface of  $\text{Pd}_{0.2}\text{Co}_{0.8}$  occurs during the electrolysis; that is, core-shell-like structure with Pd core and Co shell is generated in the ligaments.

As stated in Introduction, the dissolution of less noble element (Fe, Co or Ni in this case) in the electrolyte and the aggregation of noble adatoms (Pd in this case) through diffusion at the solid/electrolyte interface are equivalently important for the formation of nanoporous structure. Without the aggregation of Pd adatoms, the accumulated Pd atoms would block further dissolution of less noble elements after the initial dissolution at the surface, and after approximately 10 monolayers of the alloys had dissolved, the dissolution would stop and no nanopores would form.<sup>12</sup> The exposure of internal atoms of Fe, Co or Ni to  $\text{H}_2\text{SO}_4$  due to the aggregation of Pd is necessary for the subsequent dissolution of less noble elements and the formation of nanopores in remnant Pd. The EDXS and XPS (Figs. 13 and 14) suggest that the aggregation of Pd adatoms at the solid/electrolyte interfaces on  $\text{Pd}_{0.2}\text{Fe}_{0.8}$  and  $\text{Pd}_{0.2}\text{Ni}_{0.8}$  is considerably inhibited, and after the initial dissolution of Fe and Ni at the surface layers (Figs. 14(a) and (c)), Pd atoms are accumulated at the surface without exposing internal Fe and Ni to the electrolyte. As a result, no nanoporosity forms during the electrolysis, as schematically shown in Fig. 15a. On the other hand, Pd adatoms readily aggregate into islands at the solid/electrolyte interfaces on  $\text{Pd}_{0.2}\text{Co}_{0.8}$ . Similar situation is suggested for well-known nanoporous Au fabricated from Au-Ag alloy, where the

surface segregation of residual Ag is observed even after thorough removal of Ag by dealloying in  $\text{HNO}_3$ .<sup>48</sup> Thus, exposed Co atoms successively dissolve to the electrolyte, and consequently, nanoporosity forms in remnant Pd (Fig. 15b). These results experimentally demonstrate that the factors other than standard electrode potentials of elements in initial alloys have significant influence on occurrence or nonoccurrence of nanoporous structure in Pd.

To date, free corrosion of Pd-Co alloy for the fabrication of nanoporous Pd has not yet been successful. Figure 16 shows the FE-SEM image of the  $\text{Pd}_{0.2}\text{Co}_{0.8}$  sample after 17-day immersion in  $\text{H}_2\text{SO}_4$ . Even after 17-day immersion in the concentrated  $\text{H}_2\text{SO}_4$  electrolyte, no nanoporous structure (like Fig. 11(b)) was observed. The situation was the same when concentrated  $\text{HNO}_3$  was used instead of  $\text{H}_2\text{SO}_4$ . This is quite different from those for the free corrosion of Au-Ag alloy,<sup>12,34</sup> in which Ag readily dissolves in  $\text{HNO}_3$  or  $\text{HClO}_4$  without the electrochemical potential and nanoporous Au is spontaneously obtained. The surface segregation of Pd may be responsible for the inertness of the  $\text{Pd}_{0.2}\text{Co}_{0.8}$  alloy under free corrosion condition, although further investigation is needed to elucidate the mechanism.

It has been found that other Pd-containing alloys such as Pd-Al and Pd-Ni-P can be dealloyed to fabricate nanoporous Pd, although these initial alloys have stoichiometric intermetallic and glass phases, respectively.<sup>65,66</sup> Pd-Co alloy described above is a simple fcc binary alloy at any composition; thus the porosity can be widely



tuned by altering the composition, which is one of the advantages of Pd-Co alloy. Furthermore, combined with Co electrodeposition and thermal alloying, dealloying of Pd-Co can develop nanoporous structure on the surface of bulk Pd, increasing the surface area by up to 300 times.<sup>61</sup> Recent careful examination showed that Pd<sub>0.2</sub>Ni<sub>0.8</sub> is also a good candidate of nanoporous Pd under a limited electrochemical condition.<sup>67</sup> Raney-type Pd-Al systems can be dealloyed to nanoporous Pd as well.<sup>68-73</sup>

### 3.2 Properties: hydrogen storage

Pd is an intrinsic hydrogen-storage metal, and many studies on hydrogen storage in Pd have been conducted.<sup>74</sup> Hydrogen storage properties of nanostructured Pd such as nanocrystalline and/or nanoparticle Pd have been extensively investigated because the surface and grain boundaries are expected to offer peculiar hydrogen absorption sites. Hydrogen storage properties of nanoporous Pd are quite important because nanoporous structures obtained by dealloying are different from that of the aggregation of nanoparticles; that is, the complex surface curvature including concavity (with negative curvature) as well as convexity (with positive curvature) in nanoporous Pd may offer surface properties distinguished from those of nanoparticles. This section briefly describes the hydrogen storage properties of nanoporous Pd.<sup>75</sup>

Pressure-composition isotherm (PCT) measurement, which is the conventional measurement standard of hydrogen storage properties of materials, was conducted on

nanoporous Pd fabricated by dealloying Pd<sub>0.2</sub>Co<sub>0.8</sub>. Two types of nanoporous Pd, that is, as-dealloyed and annealed (at 773 K) samples, were subjected to the PCT measurements to elucidate the ligament size effect. The as-dealloyed and annealed samples had average ligament diameters of 20 and 140 nm, respectively (Fig. 17).

5           The PCT curves of the nanoporous Pd are shown in Fig. 18. The three distinct regions were found in both as-dealloyed and annealed samples. In the initial region, the H<sub>2</sub> pressure steeply increased at low hydrogen concentrations, in which H dissolves in the metallic  $\alpha$ -phase. The subsequent plateaulike region with nearly constant pressures corresponds to  $\alpha$ -to- $\beta$  phase transition. The second pressure increase region at high  
10 hydrogen concentrations indicates the H dissolution in the hydride  $\beta$ -phase. Higher measurement temperatures increased the plateau pressures in both samples, but the plateau pressures themselves were not affected by the ligament size. The as-dealloyed nanoporous Pd with a small ligament size showed a narrower miscibility gap of H between  $\alpha$ - and  $\beta$ -phases (corresponding to the storable H) than the annealed one,  
15 which is similar to that observed for the nanoparticle Pd.<sup>76,77</sup> Furthermore, the hysteresis in PCT curves of the as-dealloyed nanoporous Pd was much smaller than that of the annealed one. This vanishing trend of hysteresis in PCT curves with the decrease in ligament size is similar to that observed for Pd black.<sup>78</sup>

          The difference from the PCT behaviors of nanoparticle Pd<sup>76</sup> can be seen in the  
20 shoulders of the curves where the  $\alpha$ -to- $\beta$  phase transition starts. The hydrogen

solubility in the  $\alpha$ -phase hardly increases, although the as-dealloyed nanoporous Pd had a ligament size as small as 20 nm; that is, the shoulders of the PCTs at the initial stage are angulated. In other words, the plateau behavior can still be observed at low hydrogen concentrations in the present nanoporous Pd. This is different from the PCT behavior observed for nanoparticle Pd, where the hydrogen solubility in the  $\alpha$ -phase increases and then the shoulder becomes vague.<sup>76</sup> On the other hand, the  $\beta$ -phase formation in the present nanoporous Pd, which is shown as the second pressure increase in the PCT curves, is still similar to that observed in nanoparticle Pd, where the pressure gradually increases with hydrogen concentration. These results suggest that the nanoporous structure affects the hydrogen dissolution in Pd ( $\alpha$ -phase) and Pd-H ( $\beta$ -phase).

It is known that the H solubility in the  $\alpha$ -phase of nanocrystalline Pd<sup>79,80</sup> and nanoparticle Pd<sup>76</sup> is higher than that of bulk Pd. This is because hydrogen can dissolve at grain boundaries in nanocrystalline Pd and in the surface and subsurface regions in nanoparticle Pd, in addition to typical octahedral sites. Likewise, nanoporous Pd must have such additional sites on the surface and subsurface regions. However, the complex nanoporous structures, which have a negative curvature as well as positive one, may offer lattice expansion and contraction according to the Laplace equation.<sup>81,82</sup> When a lattice constant of metallic matrix is reduced, it becomes difficult for hydrogen to occupy interstitial sites<sup>80,83</sup> in the metallic matrix and the hydrogen solubility around

this region decreases (and vice versa). High-resolution transmission electron microscopy (HR-TEM) images of surface of nanoporous Pd are shown in Fig. 19. It is obviously observed that some crystal lattices are expanded (Fig. 19a), whereas others are contracted (Fig. 19b) near the surfaces. Dislocations are also present as shown in Fig. 19b. As exemplified in Figs. 19a and 19b, the lattices on the surface and subsurface regions are significantly disordered, although macroscopic lattice constants are almost the same as that of bulk Pd (as determined by X-ray diffraction (XRD) analyses).<sup>75</sup>

The coexistence of lattice expansion and contraction at the surface of nanoporous Pd is worth noting. To elucidate the effect of lattice constants on the hydrogen adsorption behavior on the Pd surface, first-principles calculations were conducted. The calculations revealed the relationship between hydrogen adsorption energy  $\Delta E_{ad}$  and lattice strain  $\varepsilon$ , as shown in Fig. 20. The absolute value of  $\Delta E_{ad}$  increases with  $\varepsilon$ . This monotonic relationship between  $\Delta E_{ad}$  and  $\varepsilon$  suggests that lattice expansion and contraction, in the range of  $-0.05 < \varepsilon < +0.05$ , promotes and inhibits the hydrogen adsorption on the Pd (111) surface, respectively. Comparison of density of states (DOS) for the H-adsorbed surface models with different lattice strains (Fig. 21) shows that hydrogen adsorption induces a split-off state below the Pd  $4d$  band. In particular, Fig. 21 reveals that the energy difference ( $\delta\varepsilon$ ) between the bottom of the Pd band and the split-off H-Pd bonding state monotonically increases with lattice strain  $\varepsilon$ . The

energy difference  $\delta\varepsilon$  is closely related to the bond strength between Pd surface and adsorbed H.<sup>84</sup> Thus this result is in good agreement with the trend of the hydrogen adsorption energy  $\Delta E_{\text{ad}}$ . These calculations qualitatively indicate that the hydrogen dissolves more preferably on Pd surfaces with larger lattice strain.

5           The nanoporous Pd has surface lattice disorder including both lattice expansion and contraction. Lattice expansion enhances the hydrogen solubility at the surface; however, lattice contraction reduces the solubility. These effects cancel each other in the nanoporous Pd owing to the coexistence of the lattice expansion and contraction. The resulting total hydrogen solubility in the  $\alpha$ -phase of nanoporous Pd may be nearly  
10 the same as that of bulk Pd. Thus, unique PCT behaviors of the nanoporous Pd seems to be much related to the complex nanoporous structure.

#### **4. Nanoporous nickel and nickel-copper**

Raney-Ni and copper (Cu) with nanoporous structures have been already used as  
15 a variety of chemical catalysts.<sup>85-87</sup> Synthesis schemes of Raney-Ni and Cu catalysts are the dealloying of Ni-Al and Cu-Al alloys in alkali-leaching etchant (such as NaOH and KOH) without electrochemical potential, respectively.<sup>88,89</sup> However, nanoporous structure in Raney catalysts is irregular,<sup>85</sup> perhaps because of intermetallic compounds in the initial Ni-Al and Cu-Al alloys.

20

#### 4.1 Fabrication

Ni-manganese (Mn) binary phase diagram reveals that a single-phase solid solution of fcc Ni- $\gamma$ Mn can be produced by homogenization at a suitable temperature and subsequent rapid quenching. Furthermore, Ni-Cu-Mn ternary phase diagrams indicate that Ni, Cu and Mn form a single-phase solid solution with a wide compositional range at a high temperature. Ni and Cu are nobler elements than Mn; therefore, Mn can be readily dissolved from the starting Ni-Mn and Ni-Cu-Mn alloys, which results in the formation of nanoporous Ni and Ni-Cu.<sup>90</sup>

Figure 22 shows the anodic polarization curves for Ni<sub>0.3</sub>Mn<sub>0.7</sub>, Ni<sub>0.15</sub>Cu<sub>0.15</sub>Mn<sub>0.7</sub> and Cu<sub>0.3</sub>Mn<sub>0.7</sub> alloys measured in 1 mol/L (NH<sub>4</sub>)<sub>2</sub>SO<sub>4</sub>. The current density almost monotonically increased with the applied potential for all tested alloys. This trend is similar to the typical anodic polarization behaviors of alloys for fabrication of nanoporous metals including Pd-Co (Figs. 9 and 12). Thus, the common dealloying mechanism (described in the Introduction) is operative in the present Ni-Mn, Ni-Cu-Mn and Cu-Mn alloys in the electrolyte.

TEM images of nanoporous Ni and Ni-Cu fabricated by dealloying of Ni<sub>0.3</sub>Mn<sub>0.7</sub> and Ni<sub>0.15</sub>Cu<sub>0.15</sub>Mn<sub>0.7</sub> are shown in Fig. 23. Nanoporous structures with the typical length of approximately 10 nm can be obtained by the dealloying. Combined with XRD analyses, the ligament sizes  $d$  are estimated and plotted as a function of Ni/(Ni+Cu) molar ratio in the initial alloys in Fig. 24. It can be clearly seen that the

ligament size decreases with the increase in Ni composition. The diffusion at the solid/electrolyte interface plays a major role in nanopore coarsening. Hence, at the solid/electrolyte interface, Ni had a lower diffusivity than Cu, which results in the smaller pores and ligaments after dealloying. From another viewpoint, pore and  
5 ligament sizes of nanoporous Cu can be reduced by the addition of Ni in the initial alloy.

Thermal treatment of nanoporous Ni (preferably under reducing atmosphere) increases pore and ligament sizes up to approximately 300 nm as shown in Fig. 25. The XRD patterns of the as-processed and annealed nanoporous Ni are shown in Fig. 26,  
10 showing the peaks of metallic Ni. Inspection of the XRD patterns (Fig. 26 (b)) reveals that the diffraction angle for Ni 111 peak is significantly lowered by the nanoporous structure. As annealing temperature and thus ligament size increase, the peak angle approaches the value for bulk Ni (approximately  $44.51^\circ$  for Cu-K $\alpha$  radiation). That is, nanoporous structure as fine as 10 nm in Ni is likely to have strong effect on crystal  
15 lattice spacing, although the quantitative evaluation is difficult because of the peak broadening.

#### *4.2 Properties: magnetism in nanoporous Ni*

Nanosized materials exhibit unique magnetic properties that are greatly different  
20 from those of bulk materials. For example, it is known that nanoparticles exhibit

superparamagnetism or a very low coercivity because their coercivity strongly depends on the six power of diameter or grain size.<sup>91,92</sup> In addition, the nanosized materials often show a lower saturation magnetization than their corresponding bulk materials.<sup>93–95</sup> Nanoporous Ni fabricated by dealloying Ni-Mn is expected to have magnetic properties different from those of previous nanostructured Ni such as nanocrystalline bulk and nanoparticles owing to the complex network of nanopores and nanoligaments. The dependence of magnetic properties on the ligament size may be one of the crucial points that characterize the nanoporous structure. If the nanoporous Ni had superparamagnetism due to its extraordinarily small ligaments, it could be applied as efficient drug carrier in drug delivery system because of its porous structure might allow gradual release of drug.<sup>96</sup>

Figure 27 shows the magnetization curves of nanoporous Ni fabricated by dealloying Ni-Mn, which were measured using a vibrating sample magnetometer at room temperature.<sup>97,98</sup> These magnetization hysteresis loops are typical of ferromagnetic materials. When ligament size of nanoporous Ni is below 50 nm, the saturation magnetization ( $M_s$ ) and coercivity ( $H_c$ ) of the nanoporous Ni considerably decreased with decreasing ligament length, as summarized in Figs. 28 (a) and (b).<sup>97,98</sup> It is known that  $H_c$  of ferromagnetic nanocrystals and nanoparticles depends on  $D^6$ , where  $D$  is the grain size. However,  $H_c$  of the nanoporous Ni is proportional to  $d_L^{1.2}$ , where  $d_L$  is the ligament size, as shown in Fig. 26(a). The complex networking of



nanoligaments and nanopores may alter the dimension of exchange length, assuming that a nanoligament is the minimum unit for local magnetic anisotropy.<sup>97</sup>

As for reduced  $M_s$  in the nanoporous Ni with small ligaments, it has been known that the ferromagnetic nanoparticles also exhibit a lower  $M_s$  than the corresponding bulks.<sup>93-95</sup> Even typical ferromagnetic materials, such as Ni, can possibly be stabilized in a noncollinear magnetic order under special environments.<sup>99</sup> The spin states at the surfaces of the nanoparticles are greatly different from those of the inside. Hence, the decrease in  $M_s$  of the nanoporous Ni may be caused by the noncollinear arrangement at its surface. Furthermore, the relationship between  $M_s$  and specific surface area (Fig. 29) reveals that  $M_s$  of the nanoporous Ni tends to be lower than that of the nanoparticle Ni<sup>100</sup> when the specific surface area of the former is equal to that of the latter. This suggests that the surface effect due to the noncollinear magnetic order is enhanced in the nanoporous Ni compared with that in the nanoparticle Ni. Surface complexity in nanoporous Ni may be at least one of the reasons for higher noncollinear magnetic order.

## 5. Other nanoporous metals

Dealloying can create nanoporous structures in various metals other than Au, Pd and Ni as described above.

After the first report of fabrication of nanoporous Cu by Min et al. in 1994,<sup>101</sup>

Hayes et al. succeeded in fabricating homogeneous nanoporous Cu by dealloying a single-phase fcc Cu-Mn alloy.<sup>102</sup> Electrolytes of HCl, H<sub>2</sub>SO<sub>4</sub>, (NH<sub>4</sub>)<sub>2</sub>SO<sub>4</sub> can be used to dissolve Mn and generate nanoporous Cu. One of the promising applications of nanoporous Cu is improvement in surface-enhanced Raman scattering.<sup>103</sup>

5           Nanoporous platinum (Pt) with extraordinarily small pore and ligament sizes (< 5 nm, as shown in the TEM image in Fig. 30) can also be fabricated through the dealloying of Pt-Cu alloy where Cu dissolves in electrolytes such as H<sub>2</sub>SO<sub>4</sub>.<sup>104–106</sup> Pt-Ni alloy is another initial alloy suitable for nanoporous Pt which shows excellent oxygen reduction capacity.<sup>107</sup>

10           Furthermore, similarly to the fabrication of nanoporous Ni-Cu fabrication described above, the dealloying of ternary alloys to form nanoporous binary alloys has been attempted, and Au-Pt<sup>52</sup> and Pt-Ru<sup>108</sup> nanoporous binary alloys have been fabricated.

## 15   **6. Surface area determination**

Large surface area is one of the most prominent characteristics of nanoporous metals. Most of the peculiar properties of nanoporous metals are due to the surface irregularity, as described above; thus, determination of surface area is important. Observations by SEM and TEM can provide information of pore and ligament sizes  
20   and porosity (or relative density) etc, which may be converted to the surface area by

approximating the nanoporous structure to a certain unit cell model.<sup>33,98</sup> However, microscopic observations are always local and may lack comprehensiveness.

The Brunauer-Emmett-Teller (BET) method is one of the methods for surface area measurement of a material, in which the gas (N<sub>2</sub> for example) adsorption on the surface is detected. BET is often used to determine surface area of various nanostructured materials, including nanoporous (or mesoporous) ceramics and carbon materials. To date, there are several reports that employ BET for surface area measurement of nanoporous metals.<sup>27,109</sup> BET requires several grams of a sample in weight; however, it is sometimes difficult to prepare even one gram of nanoporous metals by dealloying in a laboratory scale. Furthermore, samples are often preheated in BET method to remove adsorptive water or contaminant, during which the actual surface area may decrease because of pore coarsening.

Alternatively, electrochemical methods are effective for surface area measurement of nanoporous metals at room temperature. Electrochemical methods require only a small amount of sample. In the electrochemical methods, the surface area is often represented by roughness factor ( $R_f$ ), which is defined as the ratio of true (or electrochemically active) surface area to apparent surface area (thus,  $R_f = 1$  for flat and smooth surface).  $R_f$  of nanoporous Au can be estimated by cyclic voltammetry (CV), using the nanoporous Au as a working electrode in H<sub>2</sub>SO<sub>4</sub>. The charge associated with the reduction of adsorbed oxygen ( $Q_{oc}$ ), which can be calculated by

the integration of the peak observed during a cathodic scan after the correction of double-layer charging in the CV, is proportional to the true surface area; thus the  $Q_{OC}$  of nanoporous Au is compared to that ( $= 390 \pm 10 \mu\text{C cm}^{-2}$ ) of the flat polycrystalline Au.<sup>110</sup> This method is applicable to nanoporous Pd as well.<sup>61,110</sup> On the other hand, the charge corresponding to hydrogen adsorption can be used to evaluate  $R_f$  of nanoporous Pt.<sup>106,110,111</sup>

Liu et al. showed another electrochemical method by utilizing underpotential deposition (UPD) of Pb for surface area measurement of nanoporous Au.<sup>112</sup> In this study, the comparison with BET method was fairly conducted on the heat-treated samples to demonstrate the availability of the proposed UPD method. Also, it was shown that the concentration of  $\text{Pb}^{2+}$  ion should be enough high to evaluate pores smaller than 8 nm.

Assessment of surface area is now gaining much importance to evaluate the catalytic and electrochemical performance of nanoporous metals. As well as peculiar properties, methods of surface area measurement must be advanced and standardized for practical use of nanoporous metals.

## 7. Summary

Nanoporous metals are currently being developed from both fundamental and application viewpoints. Dealloying is not only an important reaction related to the

corrosion of alloys, which is harmful to structural materials, but also a useful self-synthetic method for producing metallic nanoporous materials with specific functionality. The elements selected for the initial alloys must have large difference in standard electrode potential; however, in some cases (such Pd-Fe and Pe-Ni explained  
5 above) this is not a sufficient condition. There are many avenues of research that may elucidate the underlying mechanism for nanopore formation.

Ligaments and pores in nanoporous metals are as small as typical nanoparticles; thus, nanoporous metals have high surface area comparable to those of nanoparticles. In addition to the high surface area, nanoporous metals exhibit various properties  
10 different from those of nanoparticles because the complex three-dimensional network of nanoligaments and nanopores provides a different surface state from that of nanoparticles. Thus, nanoporous metals are regarded as a new type of nanostructured material emerging from nanoparticles, nanowires and nanotubes. Further functional and processing development is required for the application of these peculiar  
15 nanostructured metals.

### **Acknowledgements**

The fabrication of nanoporous Pd, Ni and Ni-Cu was financially supported by JSPS Grant-in-Aid for Scientific Research (C) (21605013). The authors thank Dr. Y.  
20 Chino, Dr. K. Tajima, Dr. K. Yoshimura (AIST, Japan) and Prof. H. Nakano

(Toyohashi University of Technology, Japan) for experimental assistance and suggestions.

## References

- 5 1. **Gibson, L. J. and Ashby, M. F.**, *Cellular Solids — Structure and Properties* (2nd Ed.), Cambridge University Press, Cambridge, 1997.
2. **Nakajima, H.**, Fabrication, properties and application of porous metals with directional pores, *Progress in Materials Science*, 52, 1091, 2007.
3. **Banhart, J.**, Manufacture, characterisation and application of cellular metals and  
10 metal foams, *Progress in Materials Science*, 46, 559, 2001.
4. **Evans, A. G., Hutchinson, J. W. and Ashby, M. F.**, Multifunctionality of cellular metal systems, *Progress in Materials Science*, 43, 171, 1998.
5. **Davis, M. E.**, Ordered porous materials for emerging applications, *Nature*, 417, 813, 2002.
- 15 6. **Corma, A.**, From microporous to mesoporous molecular sieve materials and their use in catalysis, *Chemical Reviews*, 97, 2373, 1997.
7. **Yang, P. D., Zhao, D. Y., Margolese, D. I., Chmelka, B. F. and Stucky, G. D.**, Generalized syntheses of large-pore mesoporous metal oxides with semicrystalline frameworks, *Nature*, 396, 152, 1998.
- 20 8. **Soler-Illia, G. J. de A. A., Sanchez, C., Lebeau, B. and Patarin, J.**, Chemical

strategies to design textured materials: From microporous and mesoporous oxides to nanonetworks and hierarchical structures, *Chemical Reviews*, 102, 4093, 2002.

9. **Ryoo, R., Joo, S. H., Kruk, M. and Jaroniec, M.**, Ordered mesoporous carbons, *Advanced Materials*, 13, 677, 2001.

5 10. **Lee, J., Yoon, S., Hyeon, T., Oh, S. M. and Kim, K. B.**, Synthesis of a new mesoporous carbon and its application to electrochemical double-layer capacitors, *Chemical Communications*, 21, 2177, 1999.

11. **Forty, A. J. and Durkin, P.**, A micromorphological study of the dissolution of silver-gold alloys in nitric acid, *Philosophical Magazine A*, 42, 295, 1980.

10 12. **Erlebacher, J., Aziz, M. J., Karma, A., Dimitrov, N. and Sieradzki, K.**, Evolution of nanoporosity in dealloying, *Nature*, 410, 450, 2001.

13. **Ding, Y. and Chen, M. W.**, Nanoporous metals for catalytic and optical applications, *MRS Bulletin*, 34, 569, 2009.

14. **Weissmüller, J., Newman, R. C., Jin, H.-J., Hodge, A. M. and Kysar, J. W.**,  
15 Nanoporous metals by alloy corrosion: fabrication and mechanical properties, *MRS Bulletin*, 34, 577, 2009.

15. **Raney, M.**, Method of preparing catalytic material, U. S. Patent 1,563,587, 1925.

16. **Raney, M.**, Method of producing finely-divided nickel, U. S. Patent 1,628,190, 1927.

20 17. **Wijnhoven, J. E. G. J., Zevenhuizen, S. J. M., Hendriks, M. A.**,

- Vanmaekelbergh, D., Kelly, J. J. and Vos, W. L.,** Electrochemical assembly of ordered macropores in gold, *Advanced Materials* 12, 888, 2000.
18. **Attard, G. S., Cöltner, C. G., Corker, J. M., Henke, S. and Templer, R. H.,** Liquid-crystal templates for nanostructured metals, *Angewandte Chemie International Edition in English*, 36, 1315, 1997.
19. **Hakamada, M., Yamada, Y., Nomura, T., Chen, Y., Kusuda, H. and Mabuchi, M.,** Fabrication of porous aluminum by spacer method consisting of spark plasma sintering and sodium chloride dissolution, *Materials Transactions*, 46, 2624, 2005.
20. **Kertis, F., Snyder, J., Govada, L., Khurshid, S., Chayen, N. and Erlebacher, J.,** Structure/processing relationships in the fabrication of nanoporous gold, *JOM*, 62, 50, 2010.
21. **Baker, T. A., Liu, X. and Friend, C. M.,** The mystery of gold's chemical activity: local bonding, morphology and reactivity of atomic oxygen, *Physical Chemistry Chemical Physics*, 13, 34, 2011.
- 15 22. **Zielasek, V., Jürgens, B., Schulz, C., Biener, J., Biener, M. M., Hamza, A. V. and Bäumer, M.,** Gold catalysts: nanoporous gold foams, *Angewandte Chemie International Edition*, 45, 8241, 2006.
23. **Wittstock, A., Biener, J. and Bäumer, M.,** Nanoporous gold: a new material for catalytic and sensor applications, *Physical Chemistry Chemical Physics*, 12, 12919, 20 2010.



24. **Pourbaix, M.**, *Atlas of electrochemical equilibria in aqueous solutions*, Pergamon Press, Oxford, 1966.
25. **Artymowicz, D. M., Erlebacher, J. and Newman, R. C.**, Relationship between the parting limit for de-alloying and a particular geometric high-density site percolation threshold, *Philosophical Magazine*, 89, 1663, 2009.
26. **Fritz, J. D. and Pickering, H. W.**, Selective anodic dissolution of Cu-Au alloys: TEM and current transient study, *Journal of The Electrochemical Society*, 138, 3209, 1991.
27. **Kameoka, S. and Tsai, A. P.**, CO oxidation over a fine porous gold catalyst fabricated by selective leaching from an ordered AuCu<sub>3</sub> intermetallic compound, *Catalysis Letters*, 121, 337, 2008.
28. **Zhang, Q., Wang, X. G., Qi, Z., Wang, Y. and Zhang, Z. H.**, A benign route to fabricate nanoporous gold through electrochemical dealloying of Al-Au alloys in a neutral solution, *Electrochimica Acta*, 54, 6190, 2009.
29. **Zhang, Z., Wang, Y., Qi, Z., Lin, J. and Bian, X.**, Nanoporous gold ribbons with bimodal channel size distribution by chemical dealloying of Al-Au alloys, *The Journal of Physical Chemistry C*, 113, 1308, 2009.
30. **Hakamada, M. and Mabuchi, M.**, Nanoporous gold prism microassembly through a self-organizing route, *Nano Letters*, 6, 882, 2006.
31. **Hakamada, M. and Mabuchi, M.**, Mechanical strength of nanoporous gold

fabricated by dealloying, *Scripta Materialia*, 56, 1003, 2007.

32. **Hakamada, M. and Mabuchi, M.**, Thermal coarsening of nanoporous gold: melting or recrystallization, *Journal of Materials Research*, 24, 301, 2009.

33. **Hakamada, M., Chino, Y. and Mabuchi, M.**, Nanoporous surface fabricated on  
5 metal sheets by alloying/dealloying technique, *Materials Letters*, 64, 2341, 2010.

34. **Ding, Y., Kim, Y.-J. and Erlebacher, J.**, Nanoporous gold leaf: “Ancient technology”/ Advanced material, *Advanced Materials*, 16, 1897, 2004.

35. **Qian, L. H. and Chen, M. W.**, Ultrafine nanoporous gold by low-temperature dealloying and kinetics of nanopore formation, *Applied Physics Letters*, 91, 083105,  
10 2007.

36. **Parida, S., Kramer, D., Volkert, C. A., Rösner, H., Erlebacher, J. and Weissmüller, J.**, Volume change during the formation of nanoporous gold by dealloying, *Physical Review Letters*, 97, 035504, 2006.

37. **Snyder, J., Livi, K. and Erlebacher, J.**, Dealloying silver/gold alloys in neutral  
15 silver nitrate solution: porosity evolution, surface composition, and surface oxides, *Journal of the Electrochemical Society*, 155, C464, 2008.

38. **Liu, Y., Bliznakov, S. and Dimitrov, N.**, Factors controlling the less noble metal retention in nanoporous structures processed by electrochemical dealloying, *Journal of the Electrochemical Society*, 157, K168, 2010.

20 39. **Li, R. and Sieradzki, K.**, Ductile-brittle transition in random porous Au, *Physical*

*Review Letters*, 68, 1168, 1992.

40. **Chen, Y. C. K., Chu, Y. S., Yi, J., McNulty, I., Shen, Q., Voorhees, P. W. and Dunand, D. C.**, Morphological and topological analysis of coarsened nanoporous gold by x-ray nanotomography, *Applied Physics Letters* 96, 043122, 2010.

5 41. **Nanda, K. K., Sahu, S. N. and Behera, S. N.**, Liquid-drop model for the size-dependent melting of low-dimensional systems, *Physical Review A* 66, 013208, 2002.

42. **Biener, J., Hodge, A. M., Hamza, A. V., Hsiung, L. M. and Satcher, Jr., J. H.**, Nanoporous Au: A high yield strength material, *Journal of Applied Physics*, 97, 10 024301, 2005.

43. **Volkert, C. A., Lilleodden, E. T., Kramer, D. and Weissmüller, J.**, Approaching the theoretical strength in nanoporous Au, *Applied Physics Letters*, 89, 061920, 2006.

44. **Lee, D., Wei, X., Chen, X., Zhao, M., Jun, S. C., Hone, J., Herbert, E. G., Oliver, W. C. and Kysar, J. W.**, Microfabrication and mechanical properties of 15 nanoporous gold at the nanoscale, *Scripta Materialia*, 56, 437, 2007.

45. **Biener, J., Hodge, A. M., Hayes, J. R., Volkert, C. A., Zepeda-Ruiz, L. A., Hamza, A. V. and Abraham, F. F.**, Size effects on the mechanical behavior of nanoporous Au, *Nano Letters*, 6, 2379, 2006.

46. **Jin, H.-J., Kurmanaeva, L., Schmauch, J., Rösner, H., Ivanisenko, Y. and 20 Weissmüller, J.**, Deforming nanoporous metal: Role of lattice coherency, *Acta*

*Materialia*, 57, 2665, 2009.

47. **Dou, R. and Derby, B.**, Deformation mechanisms in gold nanowires and nanoporous gold, *Philosophical Magazine*, 91, 1070, 2011.

48. **Wittstock, A., Neumann, B., Schaefer, A., Dumbuya, K., Kübel, C., Biener, M.**  
5 **M., Zielasek, V., Steinrück, H. P., Gottfried J. M., Biener, J., Hamza, A. and**  
**Bäumer, M.**, Nanoporous Au: An unsupported pure gold catalyst?, *The Journal of*  
*Physical Chemistry C*, 113, 5593, 2009.

49. **Wittstock, A., Zielasek, V., Biener, J., Friend, C. M. and Bäumer, M.**,  
Nanoporous gold catalysts for selective gas-phase oxidative coupling of methanol at  
10 low temperature, *Science*, 327, 319, 2010.

50. **Haruta, M., Tsubota, S., Kobayashi, T., Kageyama, H., Genet, M. J. and**  
**Delmon, B.**, Low-temperature oxidation of CO over gold supported on TiO<sub>2</sub>,  $\alpha$ -Fe<sub>2</sub>O<sub>3</sub>,  
and Co<sub>3</sub>O<sub>4</sub>, *Journal of Catalysis*, 144, 175, 1993.

51. **Kramer, D., Viswanath, R. N. and Weissmüller, J.**, Surface-stress induced  
15 macroscopic bending of nanoporous gold cantilevers, *Nano Letters*, 4, 793, 2004.

52. **Jin, H.-J., Wang, X.-L., Parida, S., Wang, K., Seo, M. and Weissmüller, J.**,  
Nanoporous Au-Pt alloys as large strain electrochemical actuators, *Nano Letters*, 10,  
187, 2010.

53. **Biener, J., Wittstock, A., Zepeda-Ruiz, L. A., Biener, M. M., Zielasek, V.**,  
20 **Kramer, D., Viswanath, R. N., Weissmüller, J., Bäumer, M. and Hamza, A. V.**,

Surface-chemistry-driven actuation in nanoporous gold, *Nature Materials*, 8, 47, 2009.

54. **Weissmüller, J. Viswanath, R. N., Kramer, D., Zimmer, P., Würschum, R. and Gleiter, H.**, Charge-induced reversible strain in a metal, *Science*, 300, 312, 2003.

55. **Dixon, M. C., Daniel, T. A., Hieda, M., Smilgies, D. M., Chan, M. H. W. and Allara, D. L.**, Preparation, structure, and optical properties of nanoporous gold thin films, *Langmuir*, 23, 2414, 2007.

56. **Lang, X. Y., Guan, P. F., Zhang, L., Fujita, T. and Chen, M. W.**, Characteristic length and temperature dependence of surface enhanced Raman scattering of nanoporous gold, *The Journal of Physical Chemistry C*, 113, 10956, 2009.

57. **Qian, L. H., Inoue, A. and Chen, M. W.**, Large surface enhanced Raman scattering enhancements from fracture surfaces of nanoporous gold, *Applied Physics Letters*, 92, 093113, 2008.

58. **Kaden, W. E., Wu, T., Kunkel, W. A. and Anderson, S. L.**, Electronic structure controls reactivity of size-selected Pd clusters adsorbed on TiO<sub>2</sub> surfaces, *Science*, 326, 826, 2009.

59. **Offermans, P., Tong, H. D., van Rijn, C. J. M., Merken, P., Brongersma, S. H. and Crego-Calama, M.**, Ultralow-power hydrogen sensing with single palladium nanowires, *Applied Physics Letters*, 94, 223110, 2009.

60. **Kabius, B., Kaiser, H. and Kaesche H.**, A micromorphological study of selective dissolution of Cu from CuPd-alloys, in *Surfaces, Inhibition, and Passivation:*

*Proceedings of an International Symposium Honoring Doctor Norman Hackerman on His Seventy-Fifth Birthday*, McCafferty, E., Brodd, R. J., Eds., Electrochemical Society, Pennington, 1986, 562.

61. **Hakamada, M. and Mabuchi, M.**, Preparation of nanoporous palladium by dealloying: anodic polarization behaviors of Pd-M (M = Fe, Co, Ni) alloys, *Materials Transactions*, 50, 431, 2009.
62. **Hakamada, M. and Mabuchi, M.**, Fabrication of nanoporous palladium by dealloying and its thermal coarsening, *Journal of Alloys and Compounds*, 479, 326, 2009.
- 10 63. **Hakamada, M., Tajima, K., Yoshimura, K., Chino, Y. and Mabuchi, M.**, Solid/electrolyte interface phenomena during anodic polarization of Pd<sub>0.2</sub>M<sub>0.8</sub> (M = Fe, Co, Ni) alloys in H<sub>2</sub>SO<sub>4</sub>, *Journal of Alloys and Compounds*, 494, 309, 2010.
64. **Sieradzki, K., Dimitrov, N., Movrin, D., McCall, C., Vasiljevic, N. and Erlebacher, J.**, The dealloying critical potential, *Journal of the Electrochemical Society*, 149, B370, 2002.
- 15 65. **Wang, X., Wang, W., Qi, Z., Zhao, C., Ji, H. and Zhang, Z.**, High catalytic activity of ultrafine nanoporous palladium for electro-oxidation of methanol, ethanol, and formic acid, *Electrochemistry Communications*, 11, 1896, 2009.
66. **Yu, J., Ding, Y., Xu, C., Inoue, A., Sakurai, T. and Chen, M.**, Nanoporous metals  
20 by dealloying multicomponent metallic glass, *Chemistry in Materials*, 20, 4548, 2008.

67. **Chen, L., Guo, H., Fujita, T., Hirata, A., Zhang, W., Inoue, A. and Chen, M.,** Nanoporous PdNi bimetallic catalyst with enhanced electrocatalytic performances for electro-oxidation and oxygen reduction reactions, *Advanced Functional Materials*, 21, 4364, 2011.
- 5 68. **Wang, X., Wang, W., Qi, Z., Zhao, C., Ji, H. and Zhang, Z.,** Electrochemical catalytic activities of nanoporous palladium rod for methanol electro-oxidation, *Journal of Power Sources*, 195, 6740, 2010.
69. **Wang, X., Wang, W., Qi, Z., Zhao, C., Ji, H. and Zhang, Z.,** Fabrication, microstructure and electrocatalytic property of novel nanoporous palladium  
10 composites, *Journal of Alloys and Compounds*, 508, 463, 2010.
70. **Zhang, Q. and Zhang, Z.,** On the electrochemical dealloying of Al-based alloys in a NaCl aqueous solution, *Physical Chemistry Chemical Physics*, 12, 1453, 2010.
71. **Ji, H., Frenzei, J., Qi, Z., Wang, X., Zhao, C., Zhang, Z. and Eggeler, G.,** An ultrafine nanoporous bimetallic Ag-Pd alloy with superior catalytic activity,  
15 *CrystEngComm*, 12, 4059, 2010.
72. **Ji, H., Wang, X., Zhao, C., Zhang, C., Xu, J. and Zhang, Z.,** Formation, control and functionalization of nanoporous silver through changing dealloying media and elemental doping, *CrystEngComm*, 13, 2617, 2011.
72. **Qi, Z., Geng, H., Wang, X., Zhao, C., Ji, H., Zhang, C., Xu, J. and Zhang, Z.,**  
20 Novel nanocrystalline PdNi alloy catalyst for methanol and ethanol electro-oxidation

in alkaline media, *Journal of Power Sources*, 196, 5823, 2011.

73. **Wang, X., Wang, W., Qi, Z., Zhao, C., Ji, H. and Zhang, Z.,** Novel Raney-like nanoporous Pd catalysis with superior electrocatalytic activity towards ethanol electro-oxidation, *International Journal of Hydrogen Energy*, 37, 2579, 2012.

5 74. **McLellan, R. B. and Harkins, C. G.,** Hydrogen interactions with metals, *Materials Science and Engineering*, 18, 5, 1975.

75. **Hakamada, M., Nakano, H., Furukawa, T., Takahashi, M. and Mabuchi, M.,** Hydrogen storage properties of nanoporous palladium fabricated by dealloying, *The Journal of Physical Chemistry C*, 114, 868, 2010.

10 76. **Yamauchi, M., Ikeda, R., Kitagawa, H. and Takata, M.,** Nanosize effects on hydrogen storage in palladium, *The Journal of Physical Chemistry C*, 112, 3294, 2008.

77. **Yamauchi, M., Kobayashi, H. and Kitagawa, H.,** Hydrogen storage mediated by Pd and Pt nanoparticles, *ChemPhysChem*, 10, 2566, 2009.

78. **Everett, D. H. and Sermon, P. A.,** Crystallite size effects in the  
15 palladium/hydrogen system: a simultaneous sorption and X-ray study, *Zeitschrift für Physikalische Chemie Neue Folge*, 114, S109, 1979.

79. **Eastman, J. A., Thompson, L. J. and Kestel, B. J.,** Narrowing of the palladium-hydrogen miscibility gap in nanocrystalline palladium, *Physical Review B*, 48, 84, 1993.

20 80. **Kuji, T., Matsumura, Y., Uchida, H. and Aizawa, T.,** Hydrogen absorption of



nanocrystalline palladium, *Journal of Alloys and Compounds*, 330–332, 718, 2002.

81. **Mays, C. W., Vermaak, J. S. and Kuhlmann-Wilsdorf, D.**, On surface stress and surface tension II. Determination of the surface stress of gold, *Surface Science*, 12, 134, 1968.

5 82. **Solliard, C. and Flueli, M.**, Surface stress and size effect on the lattice parameter in small particles of gold and platinum, *Surface Science*, 156, 487, 1985.

83. **Gross, K. J., Züttel, A. and Schlapbach, L.**, On the possibility of metal hydride formation — Part II: Geometric considerations, *Journal of Alloys and Compounds*, 274, 239, 1998.

10 84. **Tománek, D., Sun, Z. and Louie, S. G.**, Ab initio calculation of chemisorption systems: H on Pd (001) and Pd (110), *Physical Review B*, 43, 4699, 1991.

85. **Robertson, S. D., Freel, J. and Anderson, R. B.**, The nature of Raney nickel VI. Transmission and scanning electron microscopy studies, *Journal of Catalysis*, 24, 130, 1972.

15 86. **Morgenstern, D. A. and Fornango, J. P.**, Low-temperature reforming of ethanol over copper-plated Raney nickel: A new route to sustainable hydrogen for transportation, *Energy and Fuels*, 19, 1708, 2005.

87. **Wainwright, M. S. and Trimm, D. L.**, Methanol synthesis and water-gas shift reactions on Raney copper catalysts, *Catalysis Today*, 23, 29, 1995.

20 88. **Qi, Z., Zhao, C., Wang, X., Lin, J., Shao, W., Zhang, Z. and Bian, X.**,

Formation and characterization of monolithic nanoporous copper by chemical dealloying of Al-Cu alloys, *Journal of Physical Chemistry C*, 113, 2009, 6694.

89. **Qi, Z., Zhang, Z., Jia, H., Qu, Y., Liu, G. and Bian, X.**, Alloy composition dependence of formation of porous Ni prepared by rapid solidification and chemical dealloying, *Journal of Alloys and Compounds*, 472, 71, 2009.

90. **Hakamada, M. and Mabuchi, M.**, Preparation of nanoporous Ni and Ni-Cu by dealloying of rolled Ni-Mn and Ni-Cu-Mn alloys, *Journal of Alloys and Compounds*, 485, 583, 2009.

91. **Herzer, G.**, Grain-size dependence of coercivity and permeability in nanocrystalline ferromagnets, *IEEE Transactions on Magnetics*, 26, 1397, 1990.

92. **Kita, E., Tsukahara, N., Sato, H., Ota, K., Yangaiharu, H., Tanimoto, H. and Ikeda, N.**, Structure and random anisotropy in single-phase Ni nanocrystals, *Applied Physics Letters*, 88, 152501, 2006.

93. **Sato, T., Iijima, T., Seki, M. and Inagaki, N.**, Magnetic-properties of ultrafine ferrite particles, *Journal of Magnetism and Magnetic Materials*, 65, 252, 1987.

94. **Gong, W., Li, H., Zhao, Z. and Chen, J.**, Ultrafine particles of Fe, Co, and Ni ferromagnetic metals, *Journal of Applied Physics*, 69, 5119, 1991.

95. **Gubbala, S., Nathani, H., Koizol, K. and Misra, R. D. K.**, Magnetic properties of nanocrystalline Ni-Zn, Zn-Mn, and Ni-Mn ferrites synthesized by reverse micelle technique, *Physica B*, 348, 317, 2004.

96. **Dames, P., Gleich, B., Flemmer, A., Hajek, K., Seidl, N., Wiekhorst, F., Eberbeck, D., Bittmann, I., Bergemann, C., Weyh, T., Trahms, L., Rosenecker, J. and Rudolph, C.**, Targeted delivery of magnetic aerosol droplets to the lung, *Nature Nanotechnology*, 2, 495, 2007.
- 5 97. **Hakamada, M., Takahashi, M., Furukawa, T. and Mabuchi, M.**, Coercivity of nanoporous Ni produced by dealloying, *Applied Physics Letters*, 94, 153105, 2009.
98. **Hakamada, M., Takahashi, M., Furukawa, T. and Mabuchi, M.**, Surface effects on saturation magnetization in nanoporous Ni, *Philosophical Magazine*, 90, 1915, 2010.
- 10 99. **Lizárraga, R., Nordström, L., Bergqvist, L., Bergman, A., Sjöstedt, E., Mohn, P. and Eriksson, O.**, Conditions for noncollinear instabilities of ferromagnetic materials, *Physical Review Letters*, 93, 107205, 2004.
100. **Chen, D.-H. and Wu, S.-H.**, Synthesis of nickel nanoparticles in water-in-oil microemulsions, *Chemistry of Materials*, 12, 1354, 2000.
- 15 101. **Min, U. S. and Li, J. C. M.**, The microstructure and dealloying kinetics of a Cu-Mn alloy, *Journal of Materials Research*, 9, 2878, 1994.
102. **Hayes, J. R., Hodge, A. M., Biener, J., Hamza, A. V. and Sieradzki, K.**, Monolithic nanoporous copper by dealloying Mn-Cu, *Journal of Materials Research*, 21, 2611, 2006.
- 20 103. **Chen, L.-U., Yu, J.-S., Fujita, T. and Chen, M. W.**, Nanoporous copper with

- tunable nanoporosity for SERS applications, *Advanced Functional Materials*, 19, 1221, 2009.
104. **Pugh, D. V., Dursun, A. and Corcoran, S. G.**, Formation of nanoporous platinum by selective dissolution of Cu from  $\text{Cu}_{0.75}\text{Pt}_{0.25}$ , *Journal of Materials Research*, 18, 216, 2003.
105. **Pugh, D. V., Dursun, A. and Corcoran, S. G.**, Electrochemical and morphological characterization of Pt-Cu dealloying, *Journal of the Electrochemical Society*, 152, B455, 2005.
106. **Liu, H., He, P., Li, Z. and Li, J.**, High surface area nanoporous platinum: Facile fabrication and electrocatalytic activity, *Nanotechnology*, 17, 2167, 2006.
107. **Snyder, J., Fujita, T., Chen, M. W. and Erlebacher, J.**, Oxygen reduction in nanoporous metal-ionic liquid composite electrocatalysts, *Nature Materials*, 9, 904, 2010.
108. **Xu, C., Wang, L., Mu, X. and Ding, Y.**, Nanoporous PtRu alloys for electrocatalysis, *Langmuir*, 26, 7437, 2010.
109. **Kameoka, S., Tsai, A. P.**, Alternately layered Au/ $\text{Fe}_3\text{O}_4$  with porous structure—a self-assembled nanoarchitecture for catalysis materials, *Journal of Materials Chemistry*, 20, 7348, 2010.
110. **Trasatti, S., Petrii, O. A.**, Real surface area measurements in electrochemistry, *Journal of Electroanalytical Chemistry*, 327, 353, 1992.

111. **Hakamada, M., Chino, Y., Mabuchi, M.,** Formation of nanoporous structure on Pt plate surface by alloying/dealloying technique, *Journal of the Japan Institute of Metals*, 75, 42, 2011.

112. **Liu, Y., Bliznakov, S., Dimitrov, N.,** Comprehensive study of the application of a Pb underpotential deposition-assisted method for surface area measurement of metallic nanoporous materials, *The Journal of Physical Chemistry C*, 113, 12362, 2009.

### Figure Captions

**Figure 1.** Schematic illustration of use of dealloying to fabricate nanoporous metals.

10 **Figure 2.** Behavior of atoms at the interface between solid and electrolyte during dealloying.

**Figure 3.** Range of controllable pore and ligament sizes controllable in nanoporous metals fabricated by dealloying.

15 **Figure 4.** Scanning electron microscopy images of nanoporous Au fabricated by free corrosion of Au-Ag alloys. Process conditions are: (a) 15 min, (b) 3 h and (c) 42 h immersion at room temperature in 70 mass% HNO<sub>3</sub> and (d) 10 h immersion at 263 K in 70 mass% HNO<sub>3</sub>. (a–c) are obtained by dealloying the stacking-rolled and annealed Au-Ag sheet surface and shown with permission from Elsevier (ref. 33). (d) is obtained from cold-rolled Au<sub>0.3</sub>Ag<sub>0.7</sub> alloy.

20 **Figure 5.** Scanning electron microscopy images of nanoporous Au fabricated by

dealloying of  $\text{Au}_{0.3}\text{Ag}_{0.7}$  alloys under electrochemical potential in 0.1 mol/L  $\text{HNO}_3$ ; (a) high-magnification image showing nanoporosity and (b) low-magnification image showing macroscopic cracks. (b) is shown with permission from American Chemical Society (ref. 30)

5 **Figure 6.** Scanning electron microscopy images of nanoporous Au sheet with 0.2 mm thickness coarsened by immersion in 35 mass% HCl solution for 24 h. (a) Top surface divided into "plots" by coarsened nanoporous walls. (b) Nanoporous walls at top surface with ligaments coarsened to 300–500 nm. (c) Bottom surface showing nanoporous structure enclosed in dense walls. (d) Tilted bottom surface showing  
10 prislake structures. Here, 'top' means the surface exposed more to HCl solution and 'bottom' means the surface which touches bottom of solution container. Shown with permission from American Chemical Society (ref. 30).

**Figure 7.** Scanning electron microscopy images of thermally treated nanoporous Au. The heating temperatures were (a) 473, (b) 573, (c) 673, (d) 773, (e) 873 and (f) 973 K  
15 and the heating time was 1800 s. Shown with permission from Materials Research Society (ref. 32).

**Figure 8.** Differential scanning calorimetry results for nanoporous Au. Shown with permission from Materials Research Society (ref. 32).

**Figure 9.** Anodic polarization curves for (a) pure Fe and  $\text{Pd}_{0.2}\text{Fe}_{0.8}$ , (b) pure Co and  $\text{Pd}_{0.2}\text{Co}_{0.8}$  and (c) pure Ni and  $\text{Pd}_{0.2}\text{Ni}_{0.8}$  in 0.1 mol/L  $\text{H}_2\text{SO}_4$ . Shown with permission  
20

from Elsevier (ref. 63).

**Figure 10.** Time variation of current during constant-potential electrolysis of Pd<sub>0.2</sub>Fe<sub>0.8</sub>, Pd<sub>0.2</sub>Co<sub>0.8</sub> and Pd<sub>0.2</sub>Ni<sub>0.8</sub>. Shown with permission from Elsevier (ref. 63).

**Figure 11.** Scanning electron microscopy images of (a) Pd<sub>0.2</sub>Fe<sub>0.8</sub>, (b) Pd<sub>0.2</sub>Co<sub>0.8</sub> and (c) Pd<sub>0.2</sub>Ni<sub>0.8</sub> after electrolysis conducted at +0.6 V (vs SCE) in 0.1 mol/L H<sub>2</sub>SO<sub>4</sub> for 1800 s at 298 K. Shown with permission from Elsevier (ref. 63).

**Figure 12.** Anodic polarization curves of Pd-Co alloys in 0.1 mol/L H<sub>2</sub>SO<sub>4</sub>. Shown with permission from The Japan Institute of Metals (ref. 61).

**Figure 13.** Energy-dispersive X-ray spectra for (a) Pd<sub>0.2</sub>Fe<sub>0.8</sub>, (b) Pd<sub>0.2</sub>Co<sub>0.8</sub> and (c) Pd<sub>0.2</sub>Ni<sub>0.8</sub> before and after electrolysis. Electrolysis was conducted at +0.6 V (vs SCE) in 0.1 mol/L H<sub>2</sub>SO<sub>4</sub> for 1800 s at 298 K. Shown with permission from Elsevier (ref. 63).

**Figure 14.** X-ray photoelectron spectra for (a,b) Pd<sub>0.2</sub>Fe<sub>0.8</sub>, (c,d) Pd<sub>0.2</sub>Co<sub>0.8</sub> and (e,f) Pd<sub>0.2</sub>Ni<sub>0.8</sub> before and after electrolysis. Electrolysis was conducted at +0.6 V (vs SCE) in 0.1 mol/L H<sub>2</sub>SO<sub>4</sub> for 1800 s at 298 K. Shown with permission from Elsevier (ref. 63).

**Figure 15.** Schematic illustration of phenomena solid/electrolyte interface consider to occur during electrolysis of (a) Pd<sub>0.2</sub>Fe<sub>0.8</sub>, Pd<sub>0.2</sub>Ni<sub>0.8</sub> and (b) Pd<sub>0.2</sub>Co<sub>0.8</sub> alloys. Shown with permission from Elsevier (ref. 63).

**Figure 16.** Scanning electron microscopy image of Pd<sub>0.2</sub>Co<sub>0.8</sub> alloy immersed in 3

mol/L H<sub>2</sub>SO<sub>4</sub> for 17 days without electrochemical potential. Shown with permission from Elsevier (ref. 62).

**Figure 17.** Scanning electron microscopy images of (a) as-dealloyed and (b) annealed nanoporous Pd. Shown with permission from American Chemical Society (ref. 75).

5 **Figure 18.** Pressure-composition isotherms for (a) as-dealloyed and (b) annealed nanoporous Pd samples. Shown with permission from American Chemical Society (ref. 75).

**Figure 19.** High-resolution transmission electron microscopy images of as-dealloyed nanoporous Pd showing (a) lattice contraction and (b) expansion. Shown with  
10 permission from American Chemical Society (ref. 75).

**Figure 20.** Relationship between hydrogen adsorption energy  $\Delta E_{ad}$  and lattice strain  $\epsilon$  calculated by first-principles calculations.

**Figure 21.** Surface electronic densities of states for H-adsorbed Pd surface models with lattice strains of (a)  $-0.05$ , (b)  $0$  and (c)  $+0.05$ . Shown with permission from  
15 American Chemical Society (ref. 75).

**Figure 22.** Anodic polarization curves of Ni-Mn, Ni-Cu-Mn and Cu-Mn alloys in 1 mol/L (NH<sub>4</sub>)<sub>2</sub>SO<sub>4</sub>. Shown with permission from Elsevier (ref. 90).

**Figure 23.** Transmission electron microscopy images of nanoporous (a) Ni and (b) Ni-Cu fabricated by dealloying of Ni-Mn and Ni-Cu-Mn alloys, respectively.

20 **Figure 24.** Relationship between ligament size and Ni/(Ni+Cu) atomic ratio of



fabricated nanoporous Ni, Ni-Cu and Cu. Error bars indicate standard deviations.

Shown with permission from Elsevier (ref. 90).

**Figure 25.** Scanning electron microscopy images of (a) as-dealloyed and (b-f) thermally treated nanoporous Ni. The heating temperatures were (b) 473, (c) 573, (d) 673, (e) 773 and (f) 873 K and the heating time was 900 s. Shown with permission from Taylor & Francis (ref. 98).

**Figure 26.** X-ray diffraction patterns in diffraction angle ranges of (a) 30–90 and (b) 43–46 degrees for as-processed and thermally treated nanoporous Ni. Shown with permission from Taylor & Francis (ref. 98).

**Figure 27.** Magnetization hysteresis loops measured at room temperature for (a) as-processed and (b–f) thermally treated nanoporous Ni. The heating temperatures were (b) 473 K, (c) 573 K, (d) 673 K, (e) 773 K and (f) 873 K. Shown with permission from Taylor & Francis (ref. 98).

**Figure 28.** Dependence of (a) coercivity ( $H_c$ ) and (b) saturation magnetization ( $M_s$ ) on ligament length ( $d_L$ ) of nanoporous Ni. Shown with permission from American Institute of Physics (ref. 97) and Taylor & Francis (ref. 98).

**Figure 29.** Variation in saturation magnetization ( $M_s$ ) as a function of specific surface area of nanoporous Ni. For reference, the saturation magnetization of a Ni nanoparticle (ref. 100) is superimposed. Shown with permission from Taylor & Francis (ref. 98).

**Figure 30.** Transmission electron microscopy image of nanoporous Pt fabricated by

dealloying Pt<sub>0.2</sub>Cu<sub>0.8</sub> in 0.1 mol/L H<sub>2</sub>SO<sub>4</sub>.

## Tables

**Table 1.** Standard electrode potentials of representative reactions of selected elements used for fabrication of nanoporous Pd.<sup>24</sup>

Element	Reaction	Standard electrode potential, $E_0$ (V vs standard hydrogen electrode)
Pd	$\text{Pd}^{2+} + 2\text{e}^- \rightarrow \text{Pd}$	+0.987
Fe	$\text{Fe}^{2+} + 2\text{e}^- \rightarrow \text{Fe}$	-0.440
Co	$\text{Co}^{2+} + 2\text{e}^- \rightarrow \text{Co}$	-0.277
Ni	$\text{Ni}^{2+} + 2\text{e}^- \rightarrow \text{Ni}$	-0.250

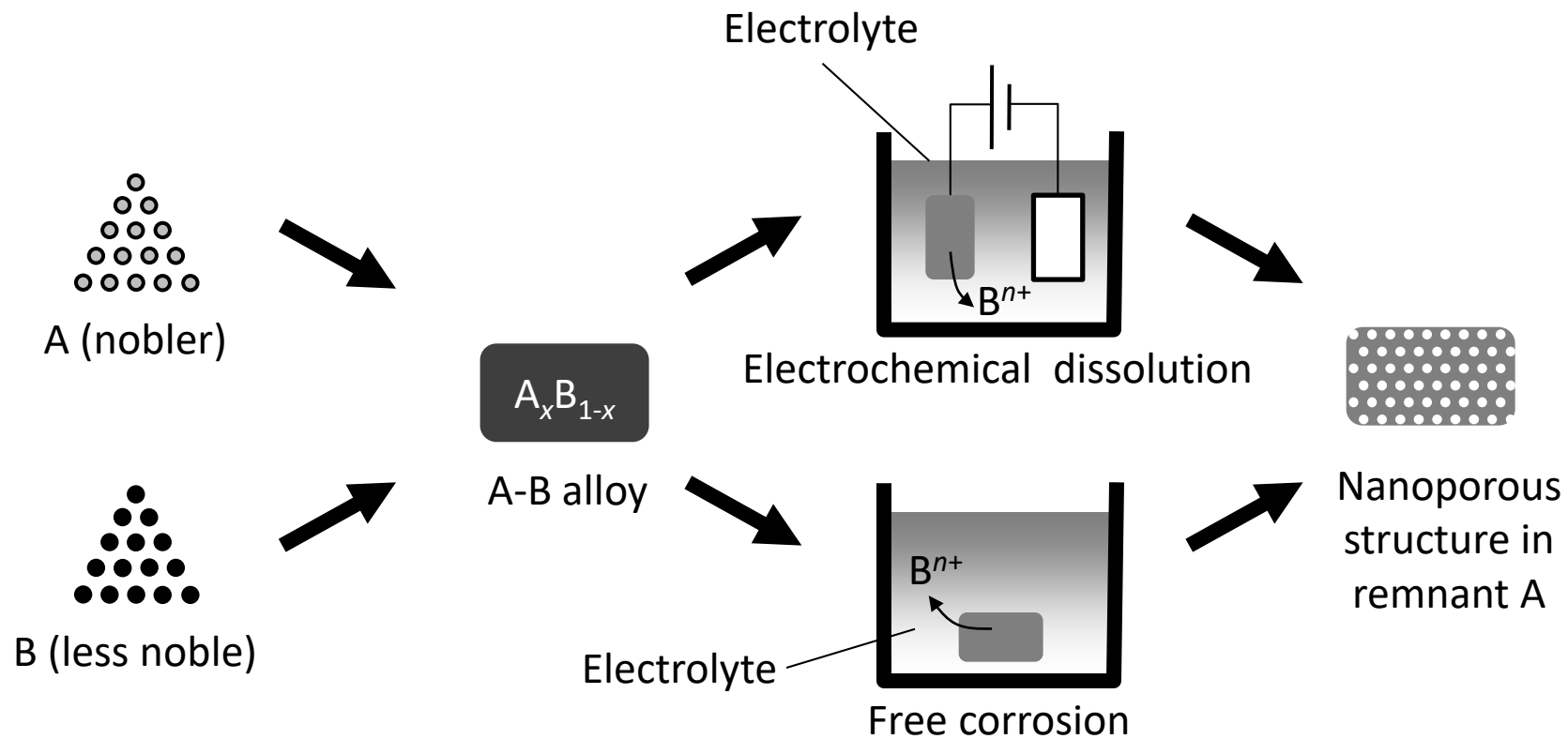


**Figure 1.** Schematic illustration of use of dealloying to fabricate nanoporous metals.

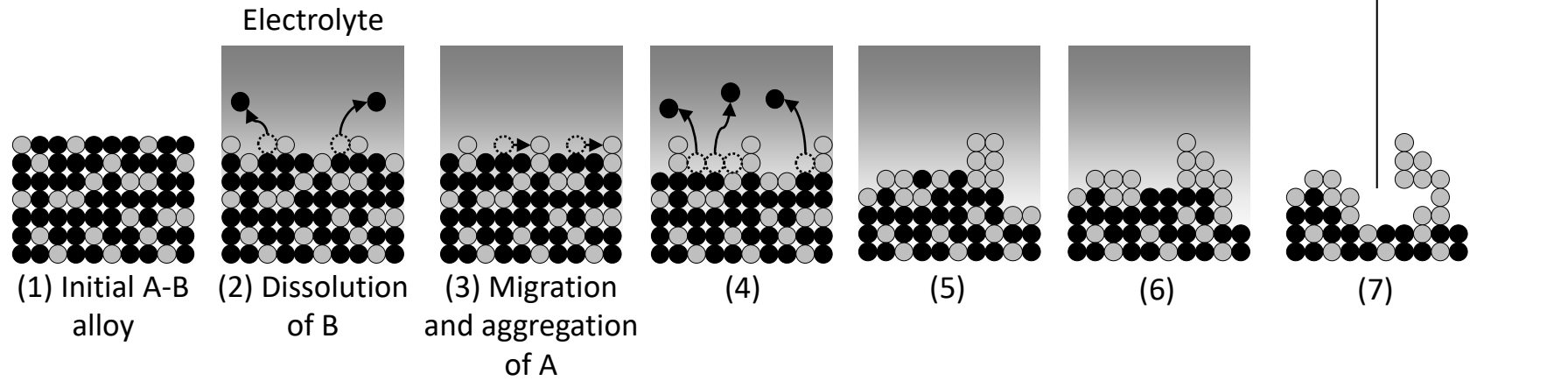
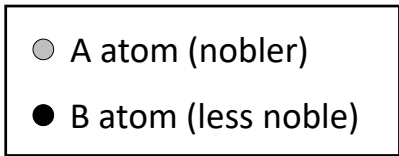


**Figure 2.** Behavior of atoms at the interface between solid and electrolyte during dealloying.

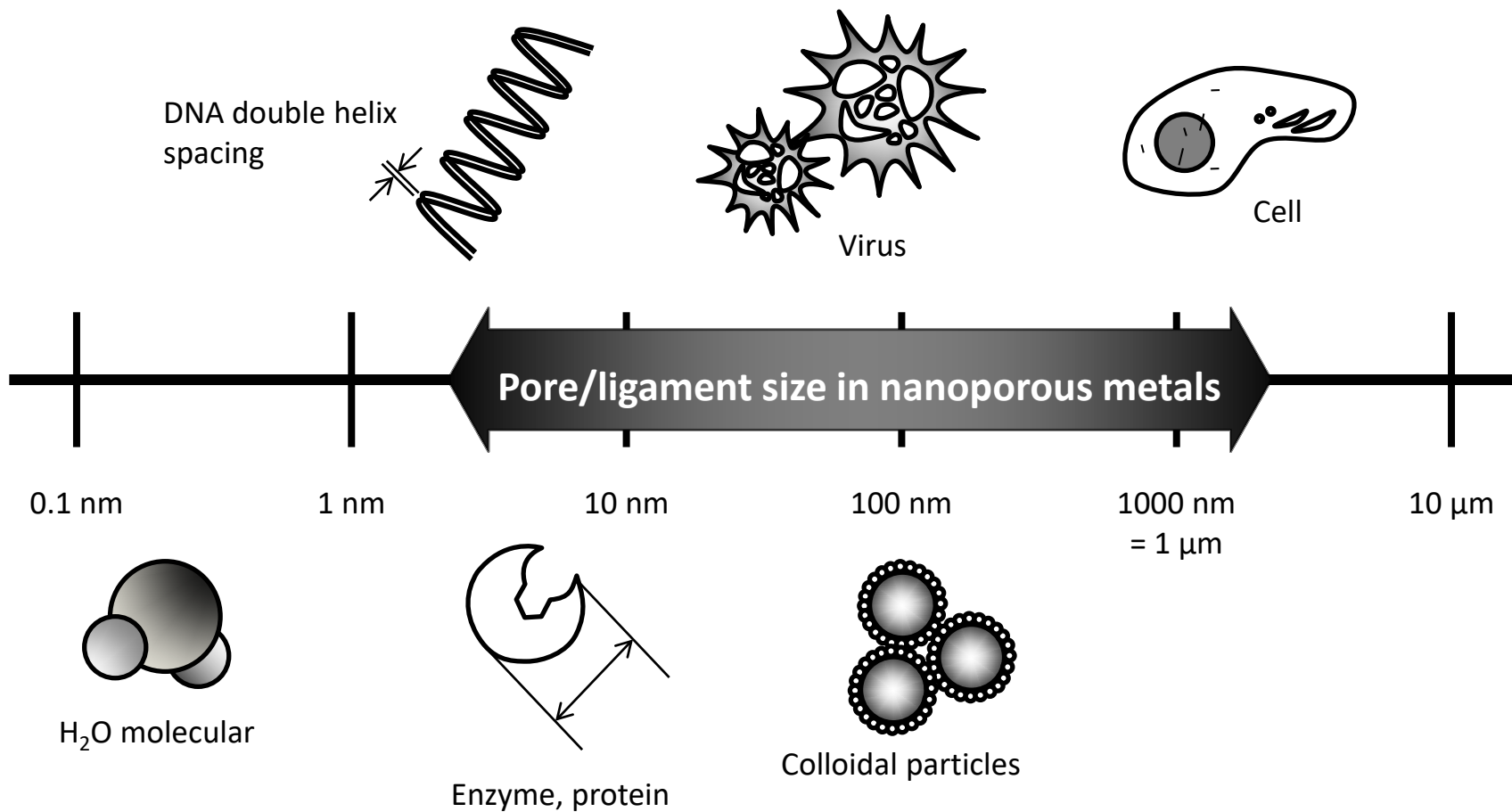


**Figure 3.** Range of controllable pore and ligament sizes controllable in nanoporous metals fabricated by dealloying.

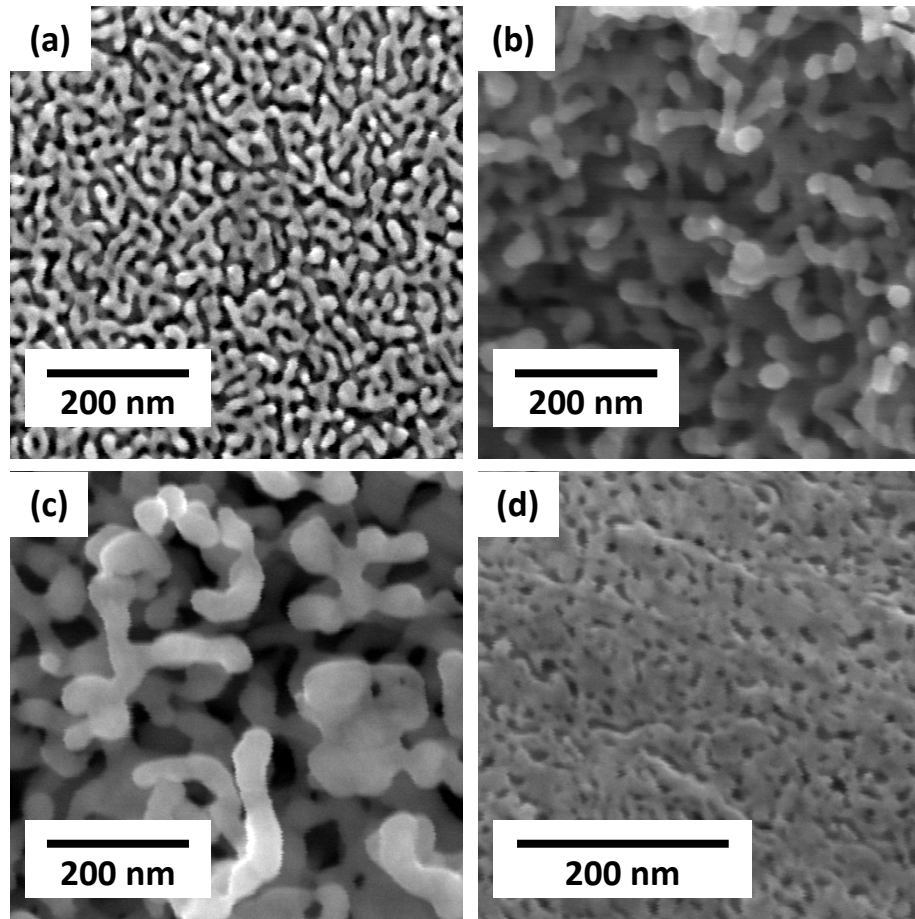


**Figure 4.** Scanning electron microscopy images of nanoporous Au fabricated by free corrosion of Au-Ag alloys. Process conditions are: (a) 15 min, (b) 3 h and (c) 42 h immersion at room temperature in 70 mass% HNO<sub>3</sub> and (d) 10 h immersion at 263 K in 70 mass% HNO<sub>3</sub>. (a–c) are obtained by dealloying the stacking-rolled and annealed Au-Ag sheet surface and shown with permission from Elsevier (ref. 33). (d) is obtained from cold-rolled Au<sub>0.3</sub>Ag<sub>0.7</sub> alloy.

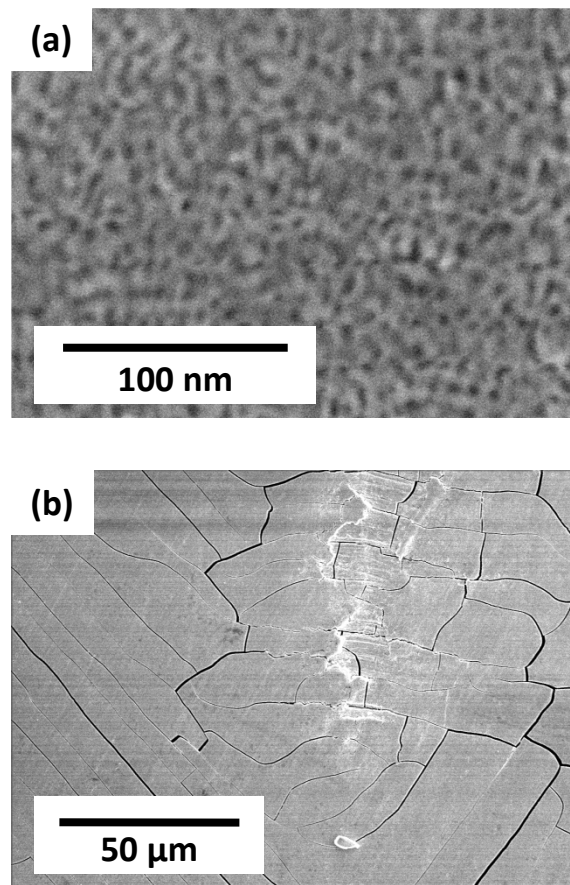


**Figure 5.** Scanning electron microscopy images of nanoporous Au fabricated by dealloying of  $\text{Au}_{0.3}\text{Ag}_{0.7}$  alloys under electrochemical potential in 0.1 mol/L  $\text{HNO}_3$ ; (a) high-magnification image showing nanoporosity and (b) low-magnification image showing macroscopic cracks. (b) is shown with permission from American Chemical Society (ref. 30).



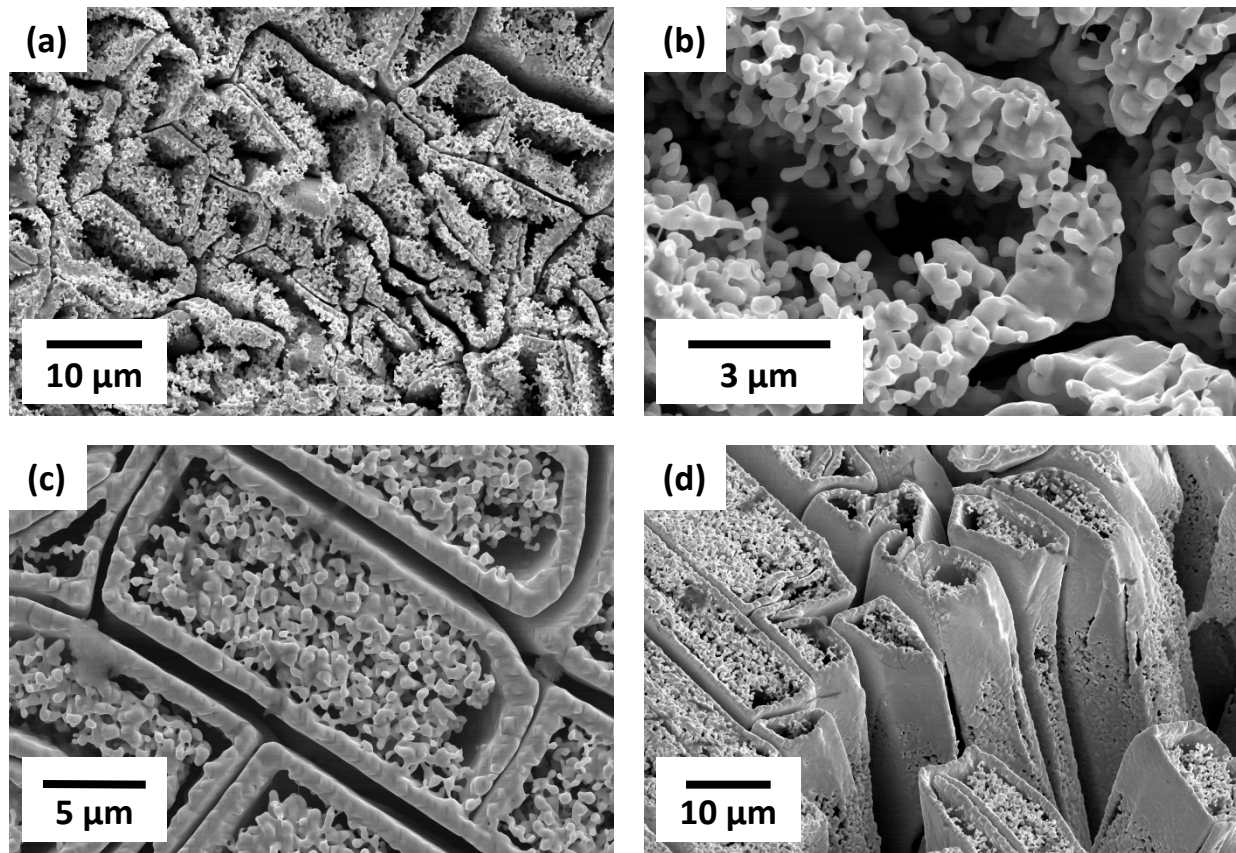


**Figure 6.** Scanning electron microscopy images of nanoporous Au sheet with 0.2 mm thickness coarsened by immersion in 35 mass% HCl solution for 24 h. (a) Top surface divided into "plots" by coarsened nanoporous walls. (b) Nanoporous walls at top surface with ligaments coarsened to 300–500 nm. (c) Bottom surface showing nanoporous structure enclosed in dense walls. (d) Tilted bottom surface showing prismatic structures. Here, 'top' means the surface exposed more to HCl solution and 'bottom' means the surface which touches bottom of solution container. Shown with permission from American Chemical Society (ref. 30).

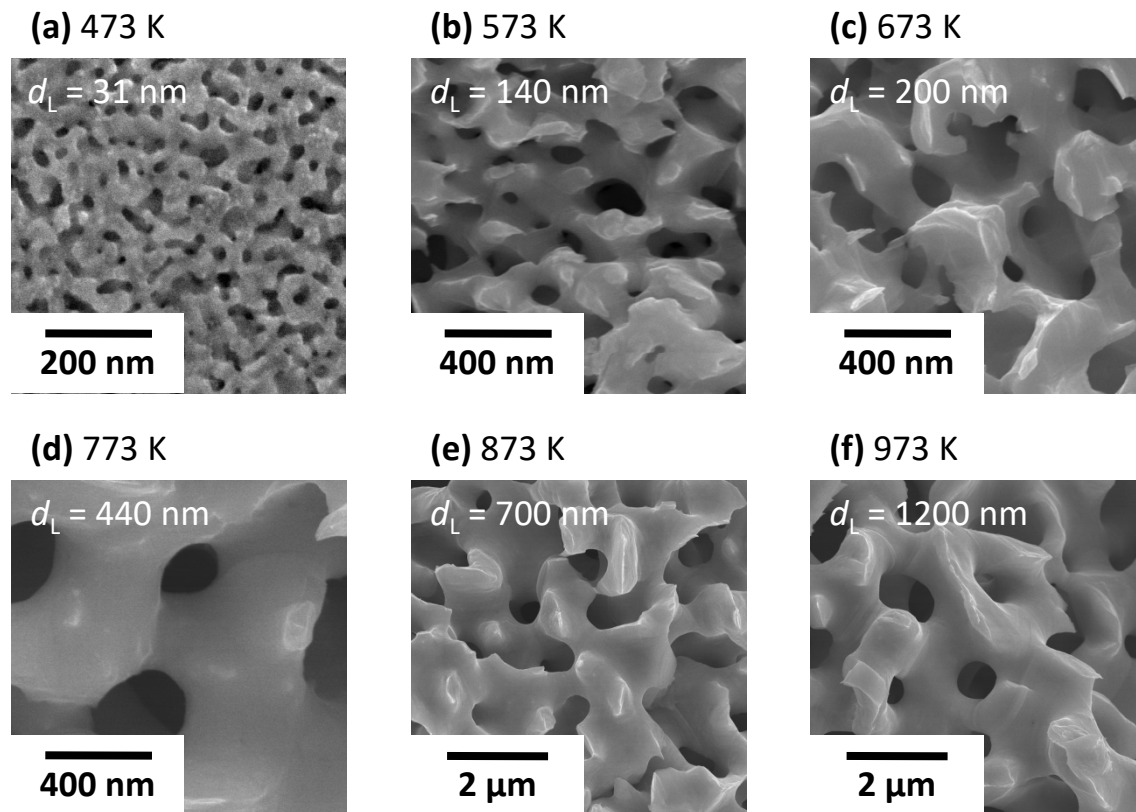


**Figure 7.** Scanning electron microscopy images of thermally treated nanoporous Au. The heating temperatures were (a) 473, (b) 573, (c) 673, (d) 773, (e) 873 and (f) 973 K and the heating time was 1800 s. Shown with permission from Materials Research Society (ref. 32).

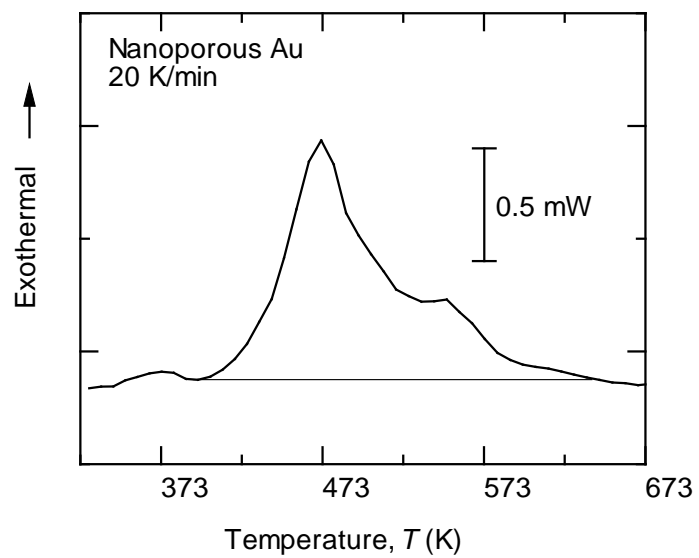


**Figure 8.** Differential scanning calorimetry results for nanoporous Au. Shown with permission from Materials Research Society (ref. 32).

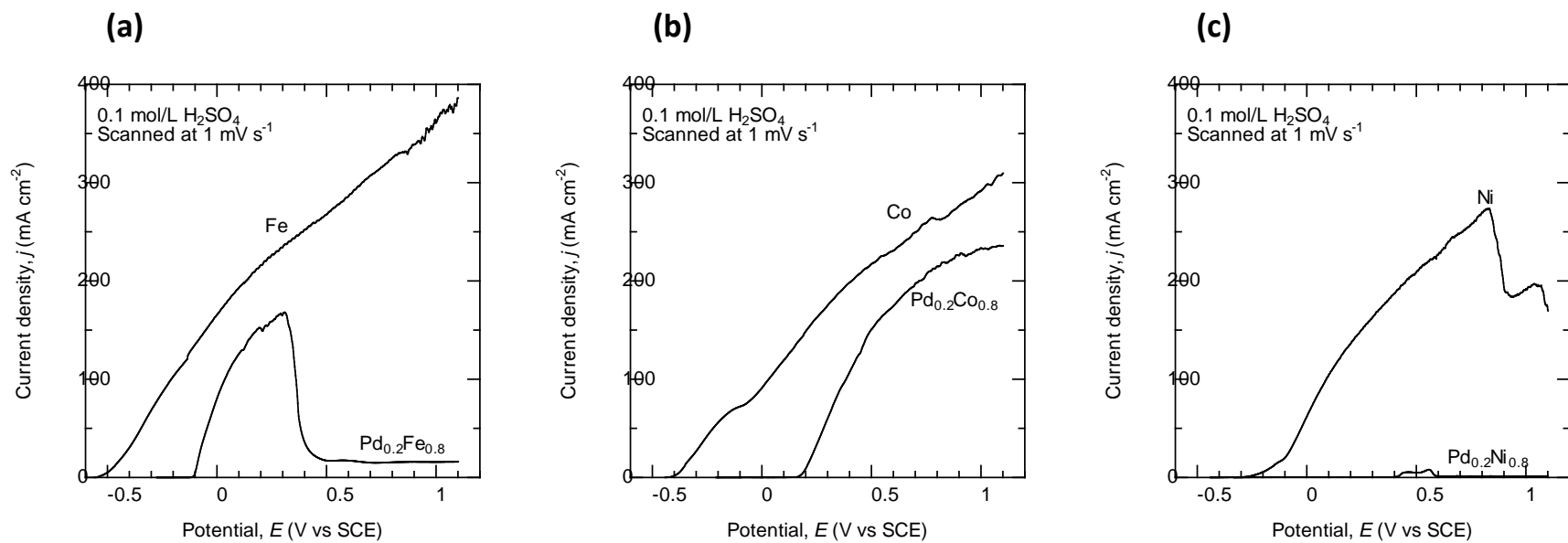


**Figure 9.** Anodic polarization curves for (a) pure Fe and Pd<sub>0.2</sub>Fe<sub>0.8</sub>, (b) pure Co and Pd<sub>0.2</sub>Co<sub>0.8</sub> and (c) pure Ni and Pd<sub>0.2</sub>Ni<sub>0.8</sub> in 0.1 mol/L H<sub>2</sub>SO<sub>4</sub>. Shown with permission from Elsevier (ref. 63).

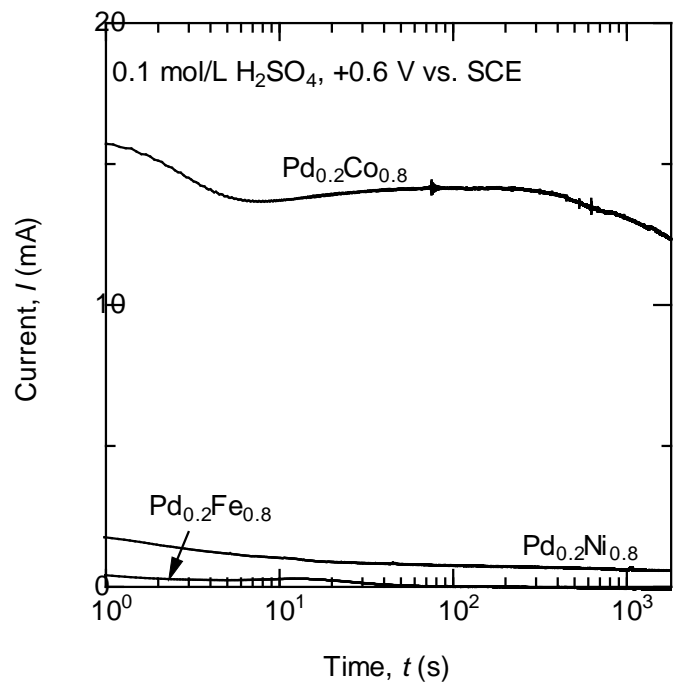


**Figure 10.** Time variation of current during constant-potential electrolysis of Pd<sub>0.2</sub>Fe<sub>0.8</sub>, Pd<sub>0.2</sub>Co<sub>0.8</sub> and Pd<sub>0.2</sub>Ni<sub>0.8</sub>. Shown with permission from Elsevier (ref. 63).

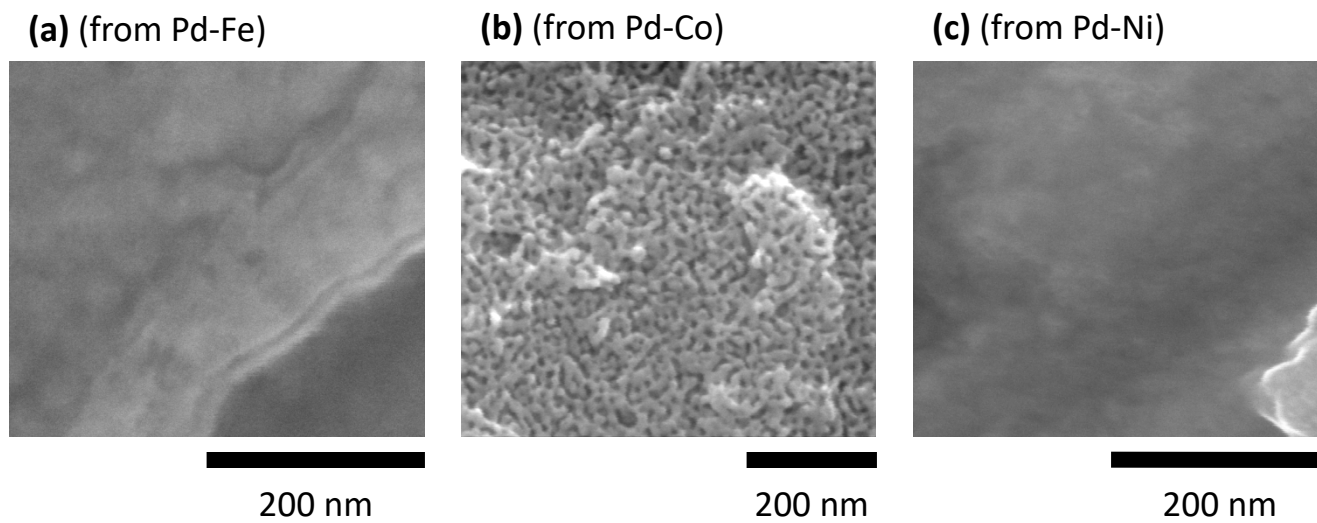


**Figure 11.** Scanning electron microscopy images of (a)  $\text{Pd}_{0.2}\text{Fe}_{0.8}$ , (b)  $\text{Pd}_{0.2}\text{Co}_{0.8}$  and (c)  $\text{Pd}_{0.2}\text{Ni}_{0.8}$  after electrolysis conducted at +0.6 V (vs SCE) in 0.1 mol/L  $\text{H}_2\text{SO}_4$  for 1800 s at 298 K. Shown with permission from Elsevier (ref. 63).

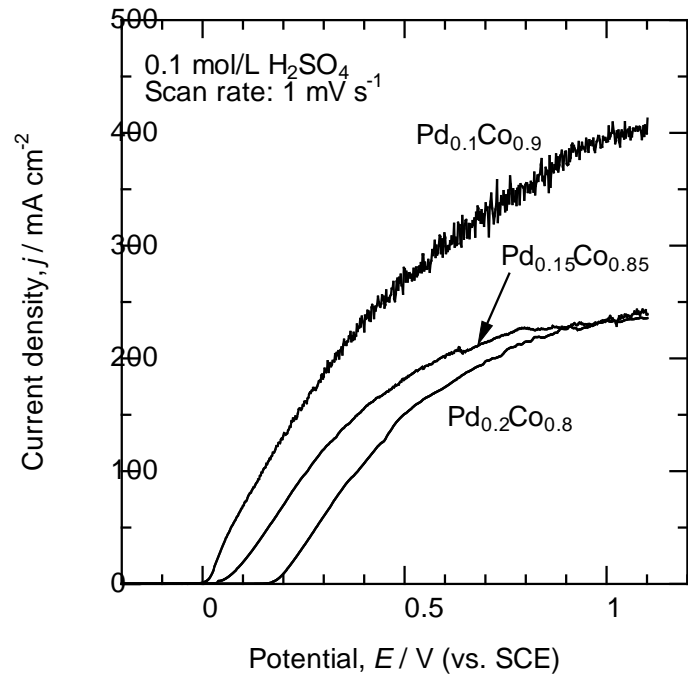


**Figure 12.** Anodic polarization curves of Pd-Co alloys in 0.1 mol/L H<sub>2</sub>SO<sub>4</sub>. Shown with permission from The Japan Institute of Metals (ref. 61).

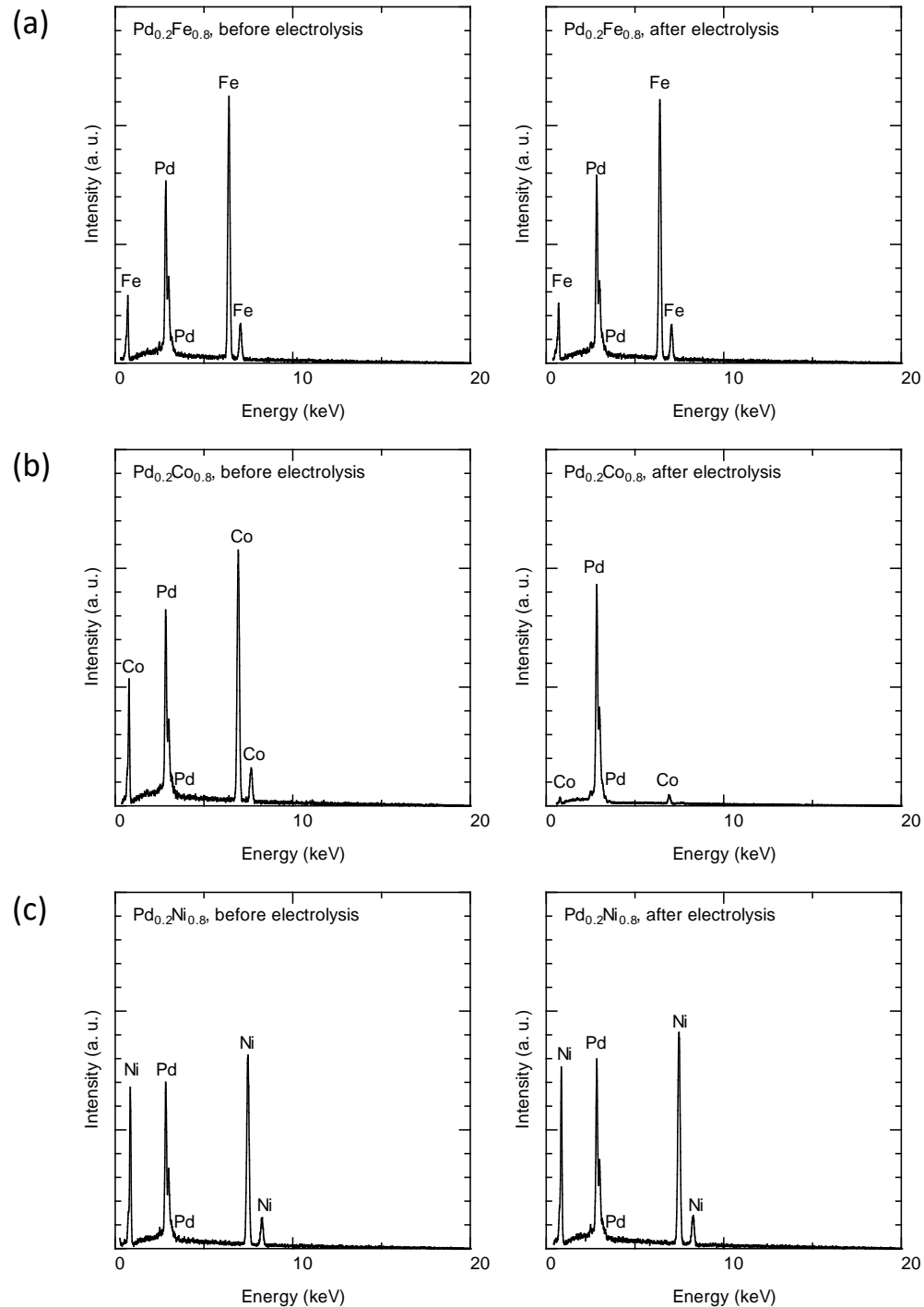


**Figure 13.** Energy-dispersive X-ray spectra for (a)  $\text{Pd}_{0.2}\text{Fe}_{0.8}$ , (b)  $\text{Pd}_{0.2}\text{Co}_{0.8}$  and (c)  $\text{Pd}_{0.2}\text{Ni}_{0.8}$  before and after electrolysis. Electrolysis was conducted at +0.6 V (vs SCE) in 0.1 mol/L  $\text{H}_2\text{SO}_4$  for 1800 s at 298 K. Shown with permission from Elsevier (ref. 63).



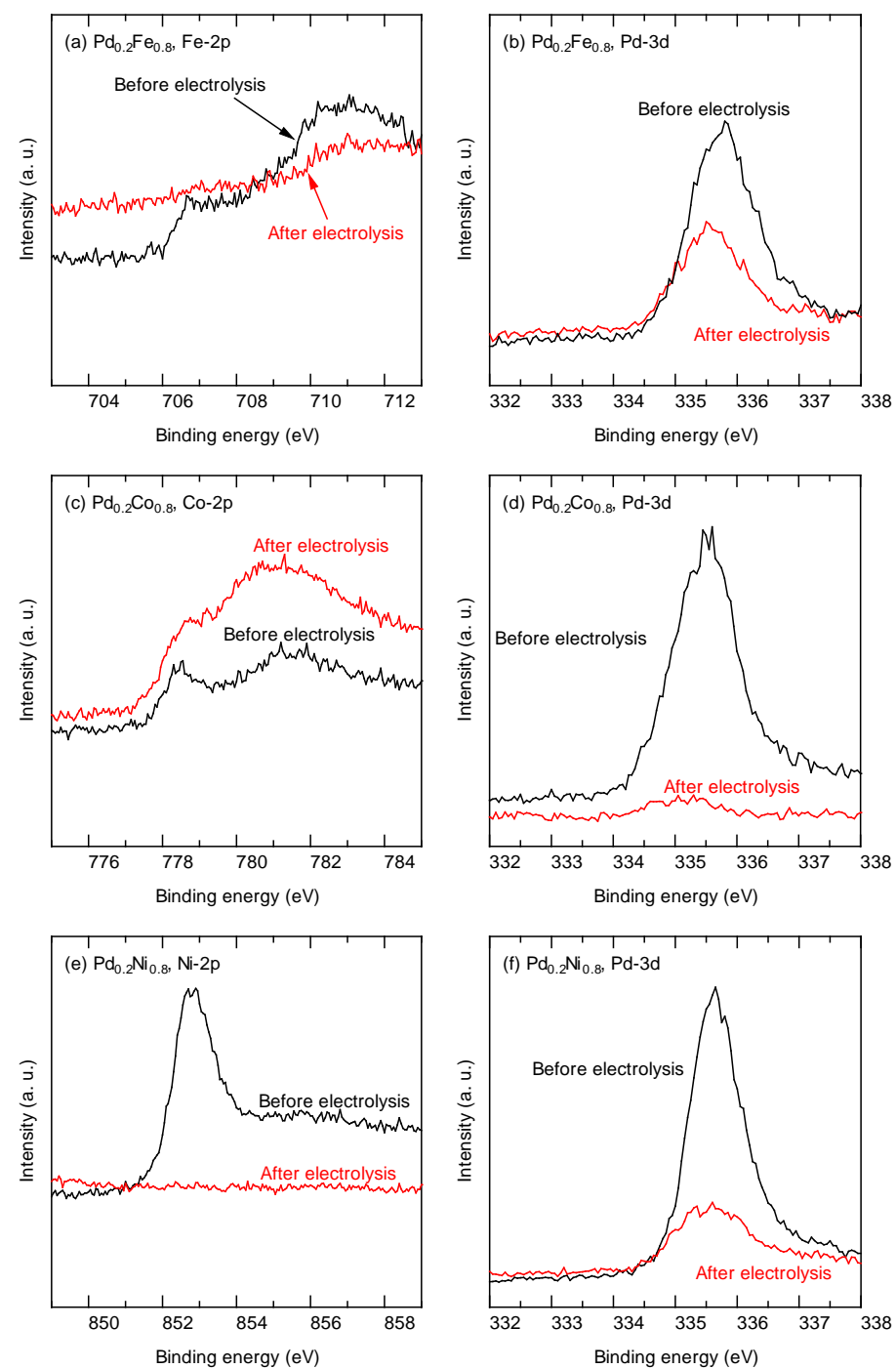


**Figure 14.** X-ray photoelectron spectra for (a,b)  $\text{Pd}_{0.2}\text{Fe}_{0.8}$ , (c,d)  $\text{Pd}_{0.2}\text{Co}_{0.8}$  and (e,f)  $\text{Pd}_{0.2}\text{Ni}_{0.8}$  before and after electrolysis. Electrolysis was conducted at +0.6 V (vs SCE) in 0.1 mol/L  $\text{H}_2\text{SO}_4$  for 1800 s at 298 K. Shown with permission from Elsevier (ref. 63).

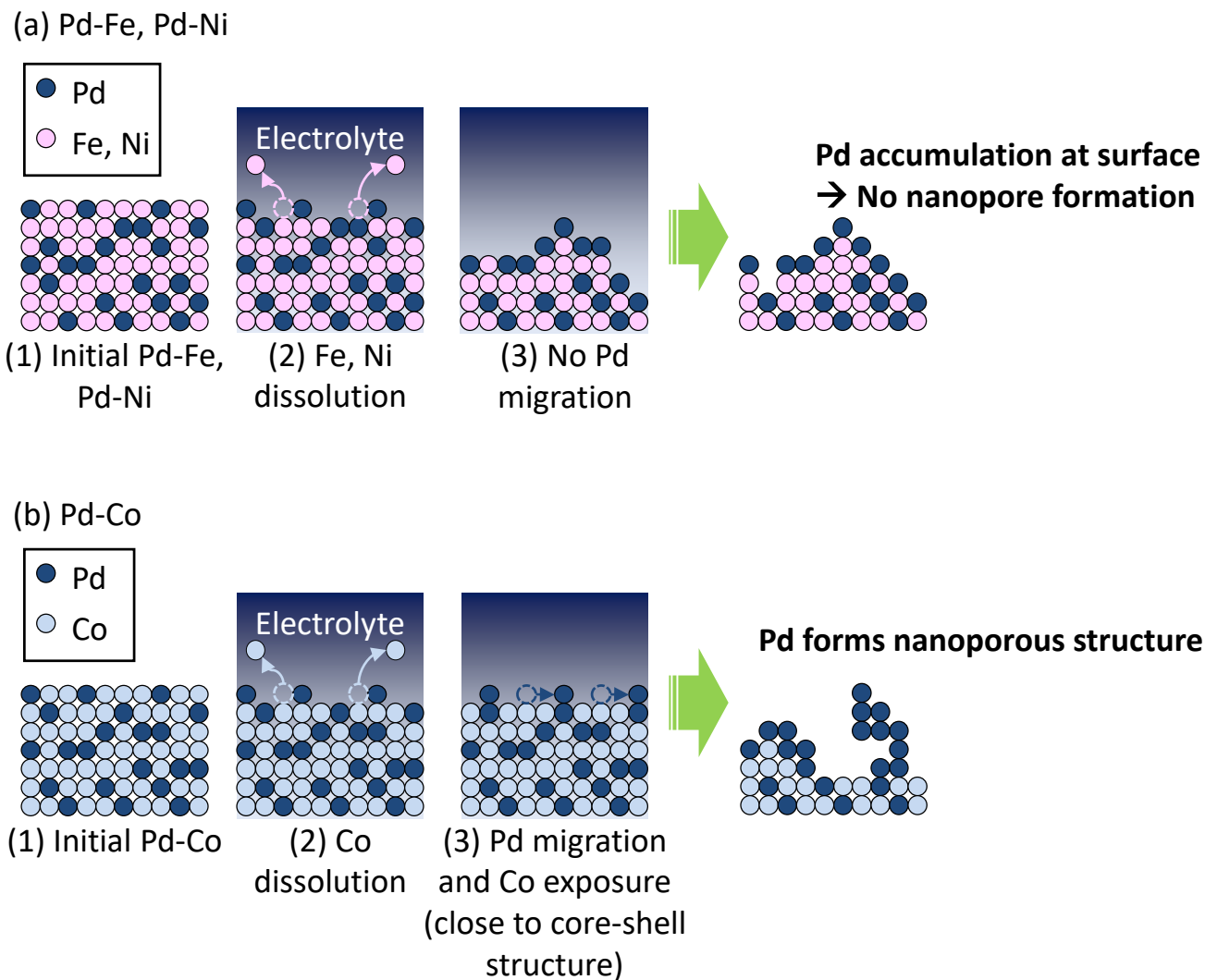


**Figure 15.** Schematic illustration of phenomena solid/electrolyte interface consider to occur during electrolysis of (a)  $\text{Pd}_{0.2}\text{Fe}_{0.8}$ ,  $\text{Pd}_{0.2}\text{Ni}_{0.8}$  and (b)  $\text{Pd}_{0.2}\text{Co}_{0.8}$  alloys. Shown with permission from Elsevier (ref. 63).

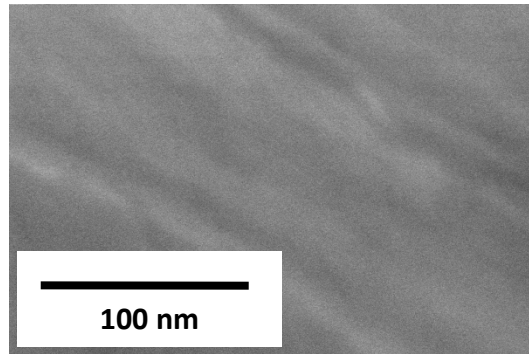
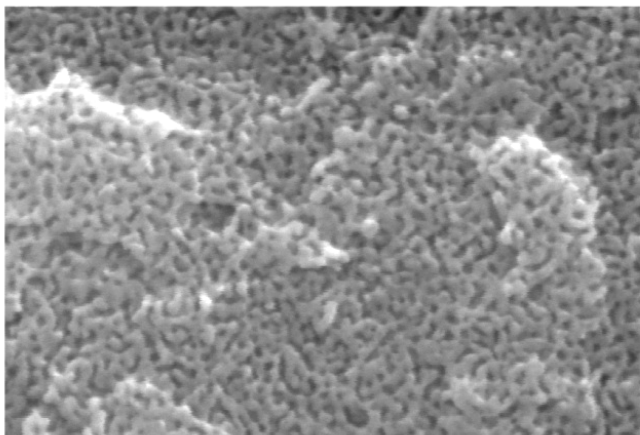


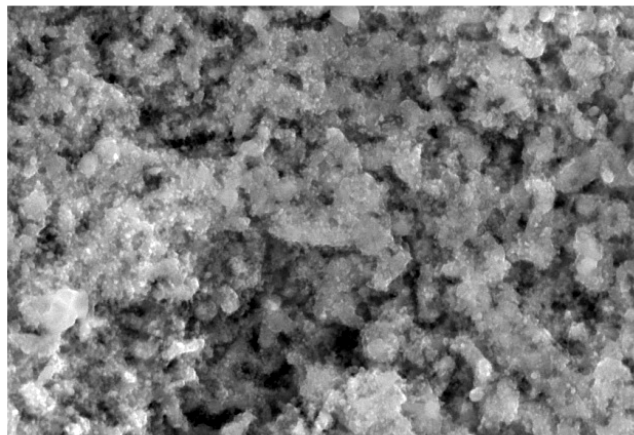
**Figure 16.** Scanning electron microscopy image of Pd<sub>0.2</sub>Co<sub>0.8</sub> alloy immersed in 3 mol/L H<sub>2</sub>SO<sub>4</sub> for 17 days without electrochemical potential. Shown with permission from Elsevier (ref. 62).

(a) As-dealloyed



200 nm

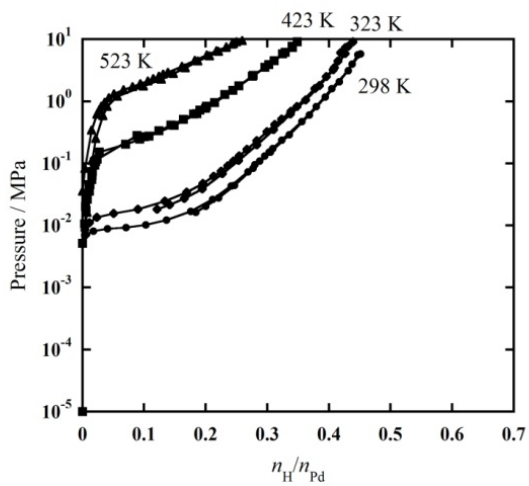
(b) Annealed



1  $\mu$ m

**Figure 17.** Scanning electron microscopy images of (a) as-dealloyed and (b) annealed nanoporous Pd. Shown with permission from American Chemical Society (ref. 75).

(a) As-dealloyed



(b) Annealed

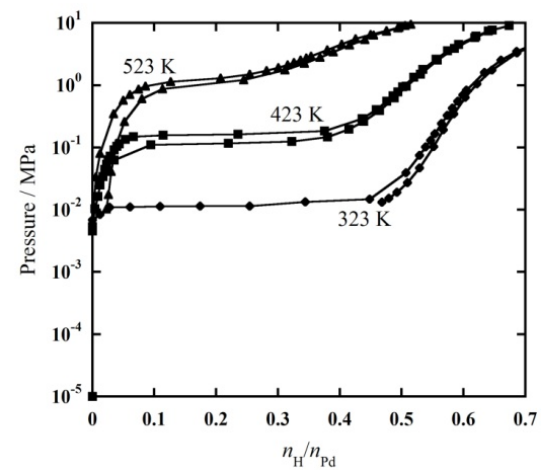


**Figure 18.** Pressure-composition isotherms for (a) as-dealloyed and (b) annealed nanoporous Pd samples. Shown with permission from American Chemical Society (ref. 75).

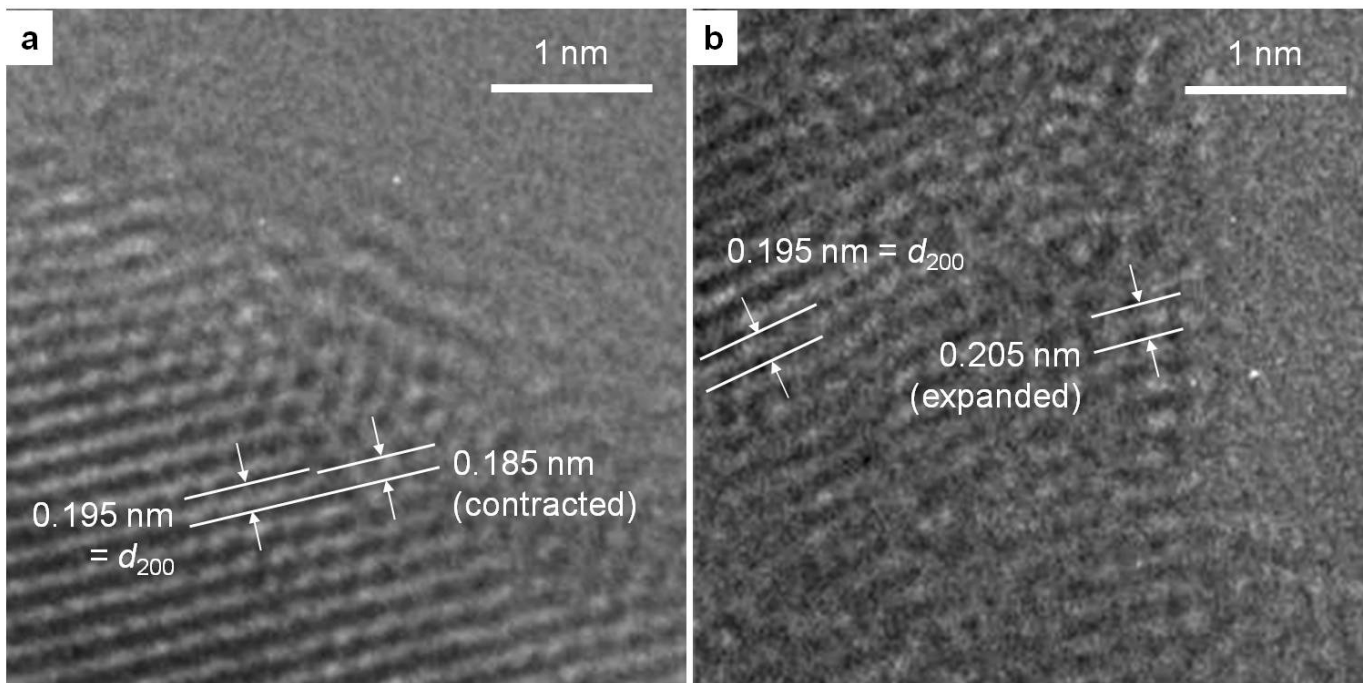


**Figure 19.** High-resolution transmission electron microscopy images of as-dealloyed nanoporous Pd showing (a) lattice contraction and (b) expansion. Shown with permission from American Chemical Society (ref. 75).

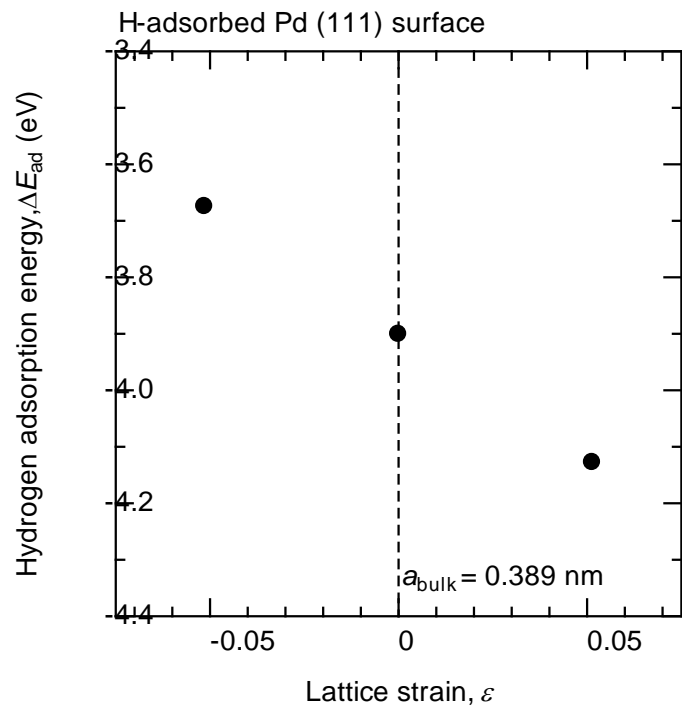


**Figure 20.** Relationship between hydrogen adsorption energy  $\Delta E_{\text{ad}}$  and lattice strain  $\varepsilon$  calculated by first-principles calculations.

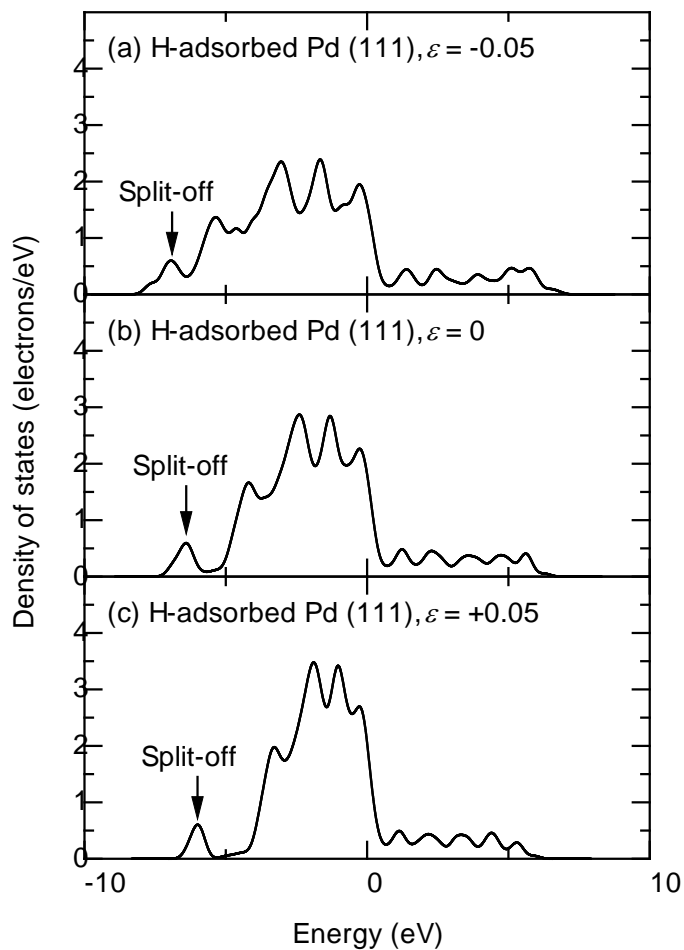


**Figure 21.** Surface electronic densities of states for H-adsorbed Pd surface models with lattice strains of (a) -0.05, (b) 0 and (c) +0.05. Shown with permission from American Chemical Society (ref. 75).



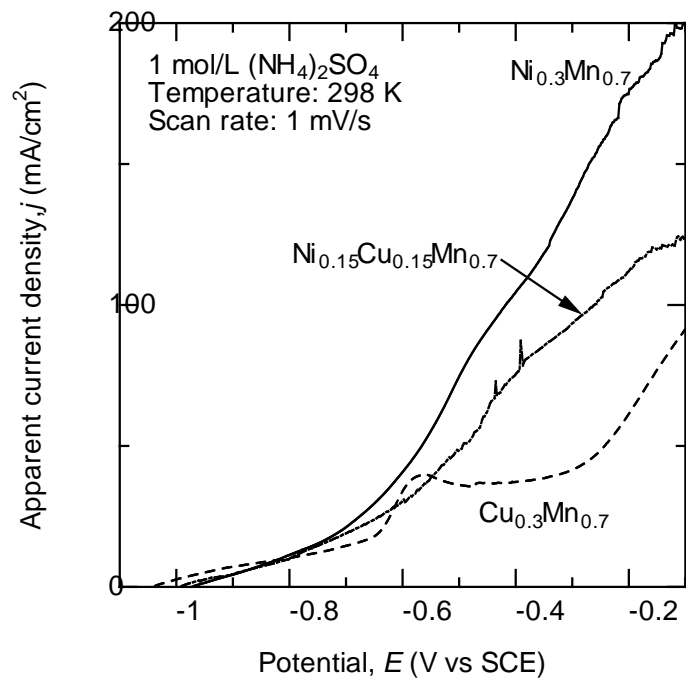
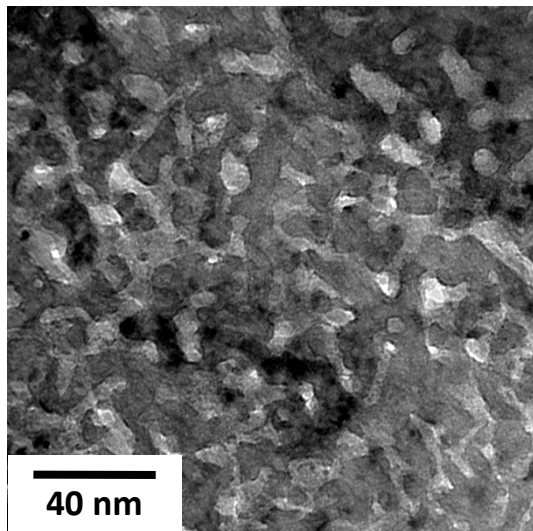


**Figure 22.** Anodic polarization curves of Ni-Mn, Ni-Cu-Mn and Cu-Mn alloys in 1 mol/L  $(\text{NH}_4)_2\text{SO}_4$ . Shown with permission from Elsevier (ref. 90).

(a) from Ni-Mn



(b) from Ni-Cu-Mn

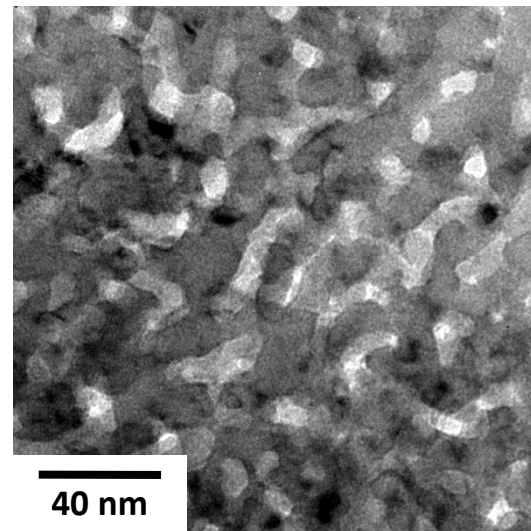


**Figure 23.** Transmission electron microscopy images of nanoporous (a) Ni and (b) Ni-Cu fabricated by dealloying of Ni-Mn and Ni-Cu-Mn alloys, respectively.

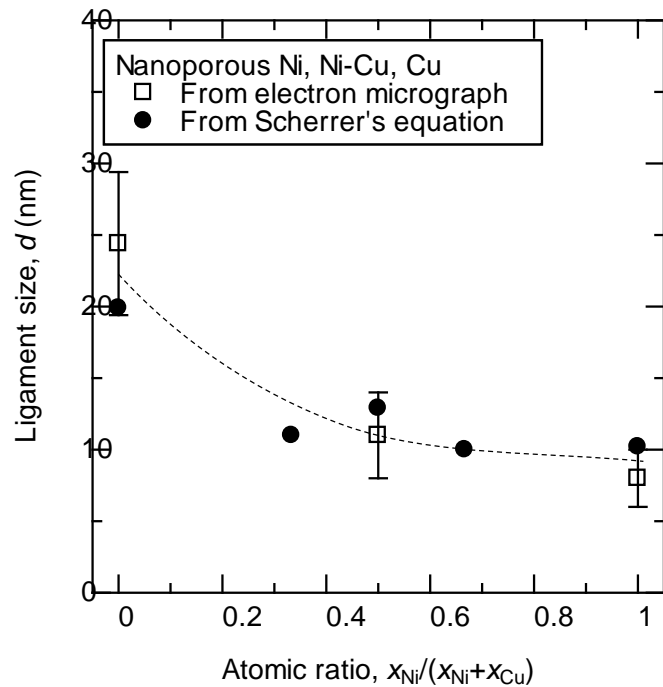


**Figure 24.** Relationship between ligament size and Ni/(Ni+Cu) atomic ratio of fabricated nanoporous Ni, Ni-Cu and Cu. Error bars indicate standard deviations. Shown with permission from Elsevier (ref. 90).

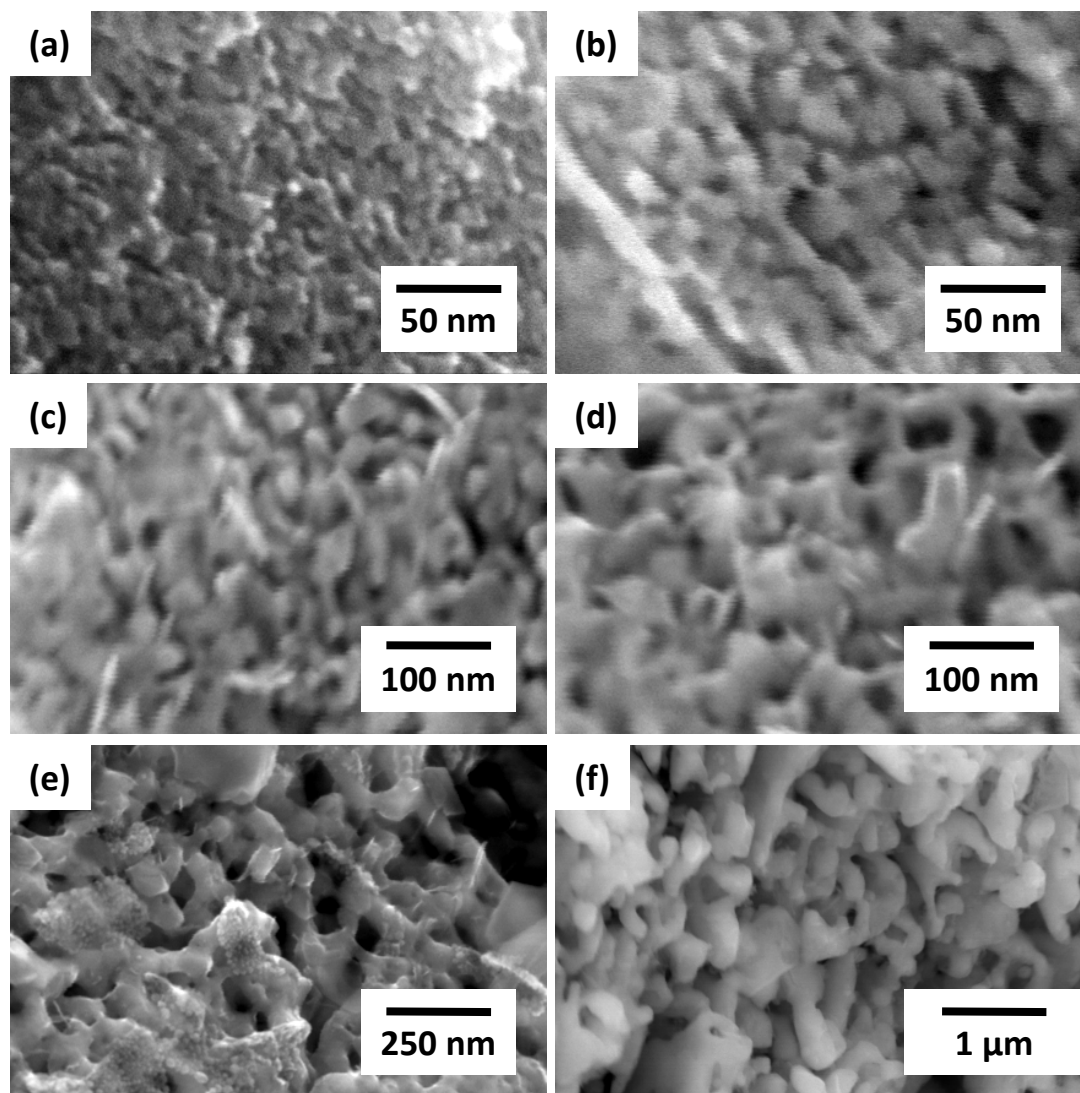


**Figure 25.** Scanning electron microscopy images of (a) as-dealloyed and (b-f) thermally treated nanoporous Ni. The heating temperatures were (b) 473, (c) 573, (d) 673, (e) 773 and (f) 873 K and the heating time was 900 s. Shown with permission from Taylor & Francis (ref. 98).

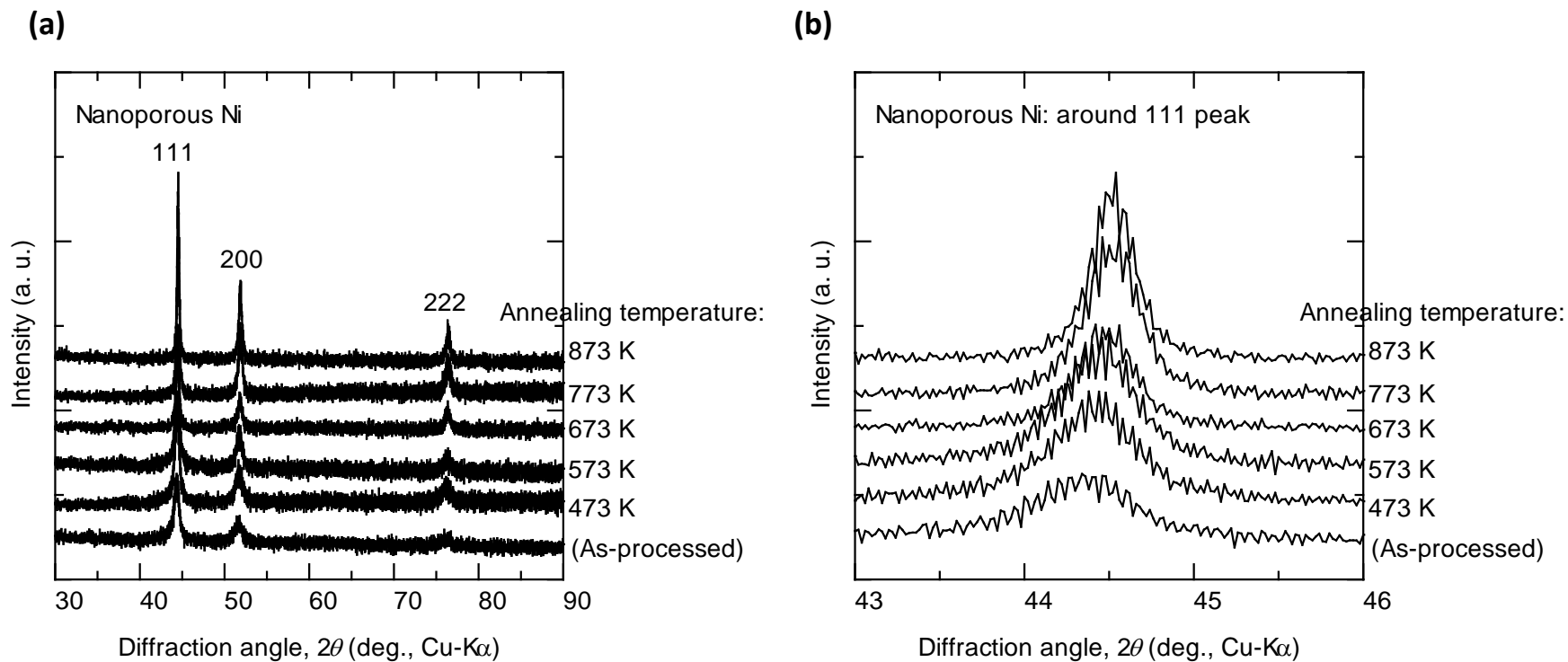


**Figure 26.** X-ray diffraction patterns in diffraction angle ranges of (a) 30–90 and (b) 43–46 degrees for as-processed and thermally treated nanoporous Ni. Shown with permission from Taylor & Francis (ref. 98).

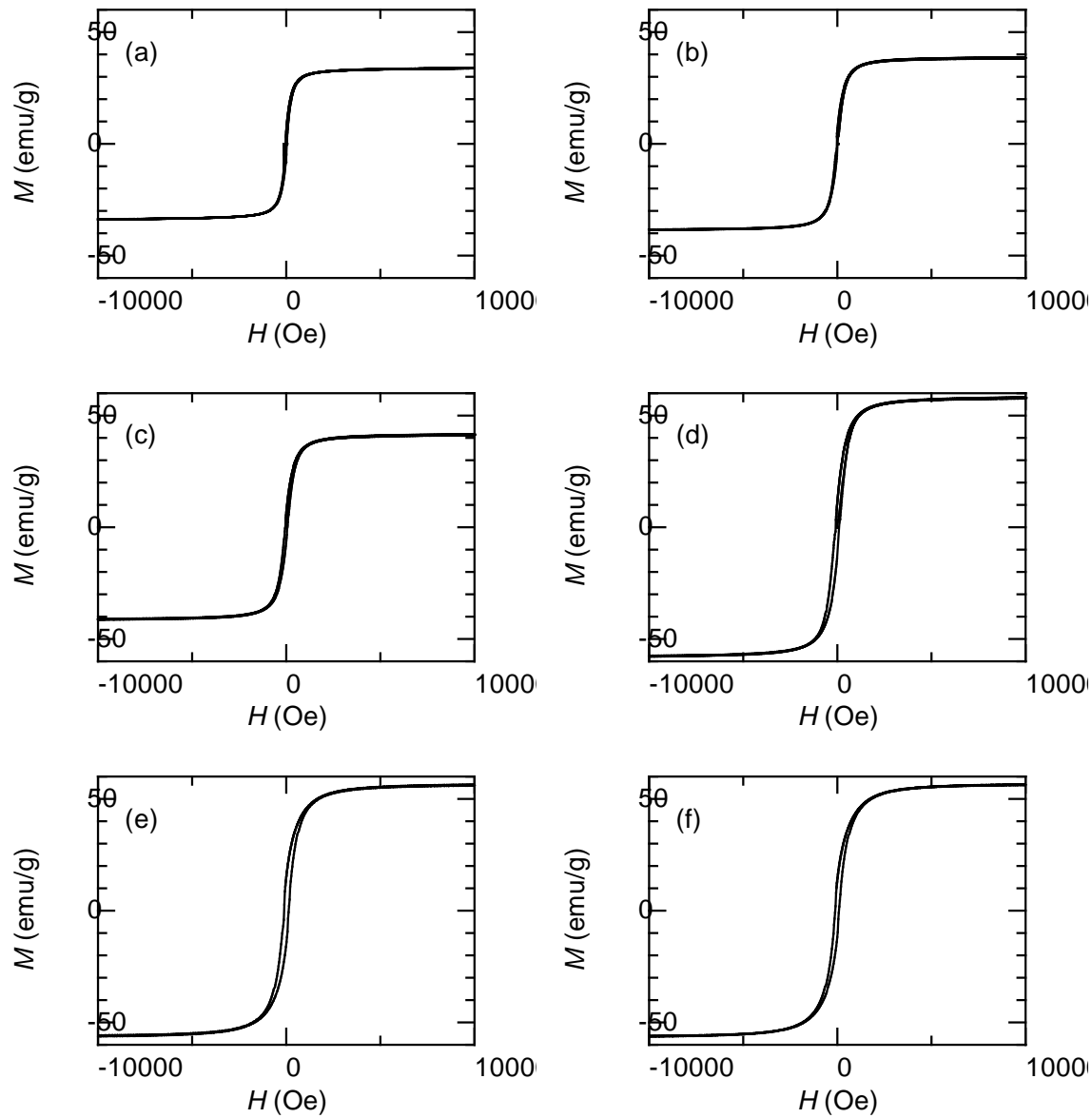


**Figure 27.** Magnetization hysteresis loops measured at room temperature for (a) as-processed and (b–f) thermally treated nanoporous Ni. The heating temperatures were (b) 473 K, (c) 573 K, (d) 673 K, (e) 773 K and (f) 873 K. Shown with permission from Taylor & Francis (ref. 98).

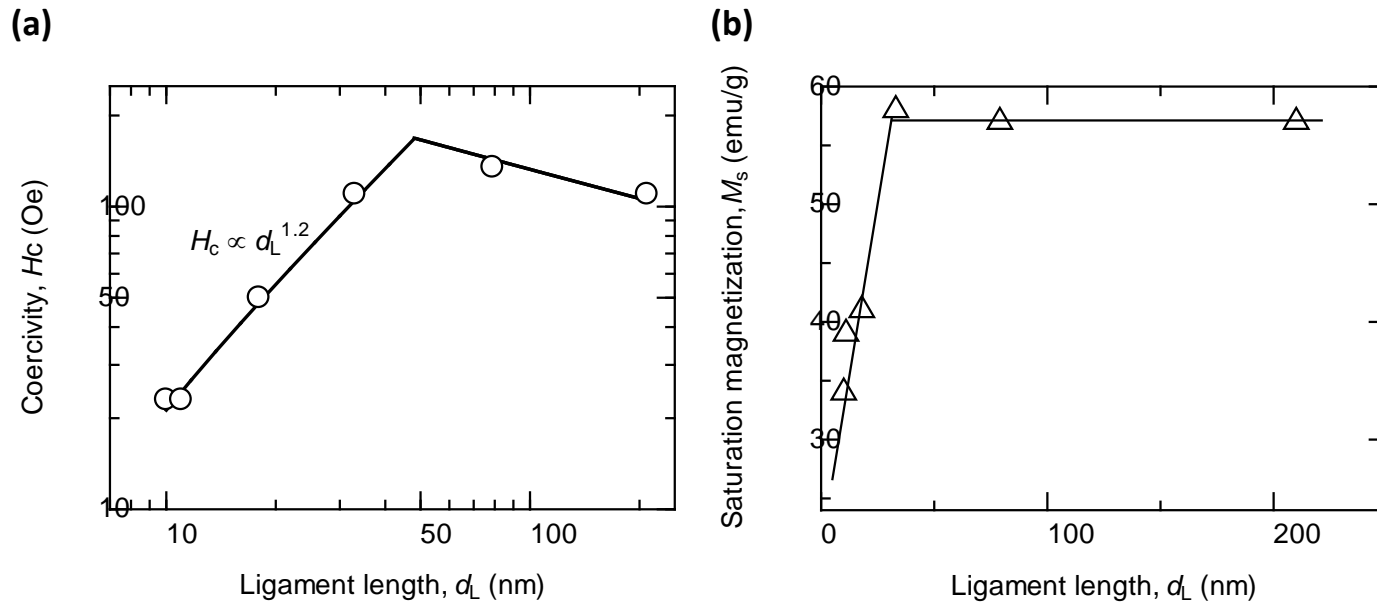


**Figure 28.** Dependence of (a) coercivity ( $H_c$ ) and (b) saturation magnetization ( $M_s$ ) on ligament length ( $d_L$ ) of nanoporous Ni. Shown with permission from American Institute of Physics (ref. 97) and Taylor & Francis (ref. 98).

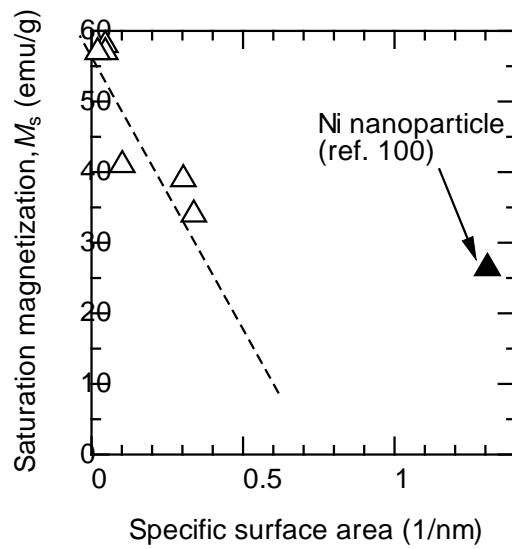
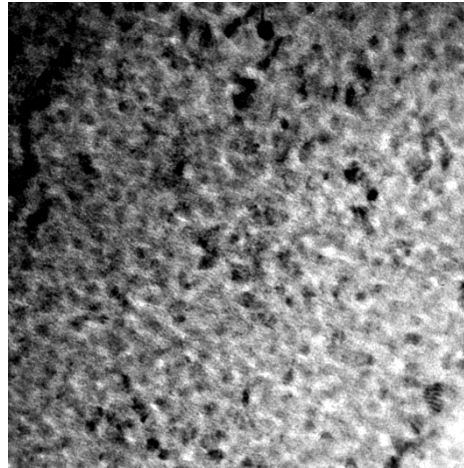


**Figure 29.** Variation in saturation magnetization ( $M_s$ ) as a function of specific surface area of nanoporous Ni. For reference, the saturation magnetization of a Ni nanoparticle (ref. 100) is superimposed. Shown with permission from Taylor & Francis (ref. 98).





50 nm

**Figure 30.** Transmission electron microscopy image of nanoporous Pt fabricated by dealloying  $\text{Pt}_{0.2}\text{Cu}_{0.8}$  in 0.1 mol/L  $\text{H}_2\text{SO}_4$ .